Cerebellar granule cell migration and folia development requires Mllt11/Af1q

Marley Blommers[1], Danielle Stanton-Turcotte[1], Emily A. Witt[1], Mohsen Heidari[1] and Angelo Iulianella[1*]

[1] Department of Medical Neuroscience, and Brain Repair Centre, Faculty of Medicine, Dalhousie University. Life Science Research Institute, 1348 Summer Street, Halifax, Nova Scotia, Canada, B3H-4R2

*Correspondence: angelo.iulianella@dal.ca

Running title: Mllt11/AF1q is required for granule cell migration during cerebellar formation

Keywords: Mllt11/Af1q, granule cells, radial migration, tangential migration, rhombic lip, foliation, Bergmann glia, anvhor points, cytoskeleton.

Contributions: MB sectioned, immunostained, imaged and analyzed the data, generated figures, and wrote the first draft. DST and EAW helped with mouse embryo and fetus generation, genotyping, and manuscript preparation. MH assisted with tissue preparation. AI supervised the project, obtained funding, edited the manuscript.

Funding: Canadian Institutes of Health Research (CIHR PJT-388914).

ABSTRACT

The organization of neurons into distinct layers, known as lamination, is a common feature of the nervous system. This process, which arises from the direct coupling of neurogenesis and neuronal migration, plays a crucial role in the development of the cerebellum, a structure exhibiting a distinct cytoarchitecture with cells arranged in discrete layers. Disruptions to neuronal migration and lamination can lead to various neurodevelopmental disorders, highlighting the significance of understanding their underlying regulators. Here, we report a role for a microtubule-interacting protein Mllt11/Af1q (Myeloid/lymphoid or mixed-lineage leukemia; translocated to chromosome 11/All1 Fused Gene From Chromosome 1q) in the migration of cerebellar granule cells (GCs). We show that Mllt11 may serve a similar role in both tangential and radial migration of excitatory GCs. Loss of *Mllt11* led to an accumulation of GC precursors in the rhombic lip region and a reduction in the number of GCs successfully populating developing folia. Consequently, this results in smaller folia and an overall reduction in cerebellar size. Furthermore, analysis of the anchoring centres reveals disruptions in the perinatal folia cytoarchitecture, including alterations in the Bergmann glia fiber orientation and reduced infolding of the Purkinje cell plate. Taken together, the findings reported herein demonstrate a role for Mllt11 in regulating neuronal migration within the developing cerebellum, which is necessary for its proper neuroanatomical organization.

INTRODUCTION

One of the fundamental questions in developmental neuroscience is how neurons navigate complex paths and settle into their proper positions within the central nervous system (CNS). During CNS development, newborn neurons need to move away from their site of origin and position themselves correctly to facilitate circuit formation and normal brain function. This tightly regulated process involves the coupling of neurogenesis with the migration of newborn neurons (Rahimi-Balaei, Bergen, Kong, & Marzban, 2018).

Neuronal migration is crucial for the development of the mammalian CNS, as it allows neurons from different proliferate zones, with distinct lineages and genetic programs, to come together and form synaptic connections (Marin, Valiente, Ge, & Tsai, 2010). This precisely controlled process involves the coordination of the cytoskeleton and its components to respond to extracellular cues. The cerebellum provides an excellent developmental model for studying the neurogenesis, neuronal migration, and assembly of neuronal circuits through lamination due to its relatively simple and highly stereotyped cytoarchitecture and numerous neuronal populations which exhibit varying modes of migration leading to its formation.

Two general modes of migration have been identified in the cerebellum: radial and tangential. Radial migration primarily occurs as newly born granule cells migrate inward, perpendicular to the pial surface, along a radial glial (RG) fiber scaffold to populate the core (Ballif et al., 2004). Tangential migration is characterized by neurons moving parallel to the brain surface, utilizing substrates other than RG, such as diffusible and membrane-bound molecules like Slits and semaphorins and precedes radial migration (Metin, Vallee, Rakic, & Bhide, 2008; Tran, Kolodkin, & Bharadwaj, 2007). In the cerebellum, granule cell precursors (GCPs) begin emerging from the Rhombic Lip (RL) around E13 and migrate tangentially in a

subpial stream over the dorsal surface of the cerebellar primordium, eventually accumulating to form the External Granule Layer (EGL) between E13 and E17.5 (Consalez, Goldowitz, Casoni, & Hawkes, 2020). GCPs give rise to granule cells (GCs), which are the most abundant neuronal population in the cerebellum. GCs represent a unique, highly migratory population that undergoes two different modes of migration during development: tangential migration to form the EGL, and radial migration from the EGL into the underlying Granule Layer (GL; Fig. 1). The switch from tangential to radial migration relies on major cytoskeletal reorganization (Chedotal, 2010). Their unique dual mode of migration and shared cellular and molecular mechanisms with migrating neurons of other brain regions makes them an ideal model in which to study neuronal migration.

Once neurons reach their site of integration, they are often organized into discrete layers, a process called lamination. Lamination is a common feature in many CNS structures, such as the neocortex, cerebellum, and retina, and it helps organize distinct cell types for information processing (Guy & Staiger, 2017; Miale & Sidman, 1961). The cerebellum is characterized by its intricate and convoluted foliation pattern and is comprised of a three-layered cortex surrounding a core of white matter (WM), consisting of distinct groups of neurons in which the formation of early-born layers provides the foundation for subsequent layers to develop upon. Along the AP axis, a sagittal section along the cerebellar midline reveals a similar basic pattern shared amongst mammals, consisting of 10 lobules (or folia; Fig. 2; (Kim et al., 2012)). These lobules are separated by distinct fissures that extend in toward the WM, increasing the surface area of the cerebellum and its capacity to accommodate a larger number of cells (Welker, 1990).

Disruption of laminar organization in the developing CNS has been implicated in disorders such as lissencephaly, periventricular nodular heterotopia, and subcortical band

heterotopia due to mispositioned neurons and altered connections (Liu, 2011). Additionally, mutations in the CXC chemokine receptor 4 (CXCR4) result in the ectopic migration of PCs in the cerebellum, leading to lamination defects and motor behavioural consequences such as poor coordination and balance (Huang et al., 2014). Similarly, defects in neuronal migration have been associated with various disorders, including brain malformation, intellectual disability, psychiatric disease, and epilepsy (Evsyukova, Plestant, & Anton, 2013; Moffat, Ka, Jung, & Kim, 2015; Stouffer, Golden, & Francis, 2016; Valiente & Marin, 2010). However, our understanding of the regulators involved in neuronal migration and cerebellar neuroanatomical organization is still incomplete.

Myeloid/lymphoid or mixed-lineage leukemia; translocated to chromosome 11 or ALL1 fused from chromosome 1q (Mllt11/Af1q; hereafter referred to as Mllt11), initially identified as an oncogene in acute myeloid leukemia, has been recognized as a novel cytoskeletal interacting protein expressed in post-mitotic neurons throughout the developing CNS (Tse, Zhu, Chen, & Cohen, 1995; Yamada, Clark, & Iulianella, 2014). Recent research has demonstrated that Mllt11 plays a role in the migration and neuritogenesis of commissural projection neurons (Stanton-Turcotte et al., 2022). Although the expression pattern of *Mllt11* has characterized in various CNS structures, its role in neural development is still being investigated (Stanton-Turcotte et al., 2022; Yamada et al., 2014). We now report a role for Mllt11 in GC migration and proper foliation of the developing cerebellum.

METHODS

Animals

All animal experiments were done according to approved protocols from the IACUC at Dalhousie University. Mice (*Mus musculus*) carrying a mutation in which the *Mllt11* locus is flanked by loxP sites (floxed) were generated as previously described (Stanton-Turcotte et al., 2022). The Ai9 *Rosa26r*^{TdTomato} reporter mouse [B6.Cg-Gt(ROSA)26Sortm9(CAG-tdTomato Hze/J, 007909), The Jackson Laboratory] was crossed into the *Mllt11*$^{flox/flox}$ strain, giving rise to *Rosa26r*$^{TdTomato/TdTomato}$*; Mllt11*$^{flox/flox}$ mice and allowing for visualization of cells that had undergone Cre-mediated excision of a floxed translational stop sequence engineered upstream of the *TdTomato* cDNA within the ubiquitously expressed *Rosa26* locus. To delete *Mllt11* within GC of the developing cerebellum, *Cux2*$^{CreERT2/+}$*; Rosa26r*$^{TdTomato/TdTomato}$ mice were crossed with the *Mllt11* floxed mice to generate *Cux2*$^{CreERT2/+}$*; Rosa26r*$^{TdTomato/TdTomato}$ control and *Cux2*$^{CreERT2/+}$*; Rosa26r*$^{TdTomato/TdTomato}$*; Mllt11*$^{flox/flox}$ conditional knockout (cKO) strains, allowing for excision of *Mllt11* and visualization of recombination events via TdTomato fluorescence in Cux2-expressing cells following tamoxifen-induced Cre activation. 100µL of Tamoxifen (20mg/mL) was administered by intraperitoneal (IP) injection at E12.5 (Fig. 3). Confirmation of *Mllt11* expression in the developing cerebellum was done using the targeted pre-floxed *Mllt11* allele, which houses a *lacZ* cassette encoding β-galactosidase. (*Mllt11*$^{tm1a(KOMP)Mbp}$). Genotyping was performed following procedures previously described (Stanton-Turcotte et al., 2022).

Histology

Timed-matings of mice were conducted to harvest brains with noon of the day of vaginal plugs taken to represent 0.5 post conception (E0.5). Pregnant dams were sacrificed by cervical

dislocation and litters were harvested at the stages described above. Embryonic brains were dissected out and fixed in 4% PFA in PB for 8 hours. Post-fixation, tissue was washed in PBS for 10 minutes and then cryoprotected in 15% and then 30% sucrose. Once equilibrated, whole brains were then embedded in optimum cutting temperature compound (OCT; Tissue-Tek, Torrance, CA) and stored at -80°C until sectioning.

Immunohistochemistry

Tissue was cryosectioned sagitally at 14µm using a Leica CM1850 cryostat with sections placed onto superfrost slides (VWR, Radnor, PA). Ten sections were mounted per sample to capture multiple axial levels on each slide. At least three animals were sectioned and analyzed for each stage. Sections were stored at -20°C until stained. Sections were first permeabilized for 10 minutes in PBS + 0.5% TritonX100 (PBT) and subsequently blocked in 3% Donkey Serum in 0.1% PBT for one hour at room temperature (RT). Sections were then incubated with primary antibodies in blocking buffer overnight at 4°C, extensively washed with PBS, and then incubated with secondary antibodies in blocking buffer at RT. Secondary antibodies were rinsed with PBS and nuclei were labeled using DAPI (4'6-diamidino-2-phenylindole; Sigma, St. Louis, MS) in PBS (1:10,000 of 3mg/mL DAPI stock: PBS) by incubation for two minutes at RT. Final PBS rises (3 x 5 minutes) followed and slides were mounted with coverslips and Dako Fluorescent Mounting Medium. The following primary antibodies were used: rabbit anti-Pax6 (1:500, Abcam), rabbit anti-Calbindin D28K (1:500, Sigma), and goat anti-Nestin (1:250, Santa Cruz). Species-specific AlexaFluor 488-, 568-, and 647-conjugated secondary antibodies (Invitrogen/ThermoFischer) were used at 1:1500 to detect primary antibodies.

In Situ Hybridization

In situ hybridization (ISH) was performed on 30µm frozen parasagittal sections obtained from E18.5 control brains fixed overnight as previously described (Yamada et al., 2014) to visualize Mllt11 mRNA in the cerebellum using an *Mllt11* riboprobe.

β-Galactosidase Staining

Mllt11 locus activity was visualized using a β-gal Tissue Stain kit (Millipore). During tissue collection, embryos (E12.5 and E14.5) or whole brains (E16.5, E18.5) were fixed for 30 minutes in fresh 4% PFA in PB, followed by 3 x 10-minute PBS rinses, and then cryoprotected and embedded using the same protocol described above. Sagittal sections were cut at 14µm and collected on slides for subsequent staining. Tissue Rinse Solutions A and B from the Tissue Stain kit (kept at 4˚C) were warmed at 37˚C in the incubation chamber and then sequentially added to slides. First, sections were rinsed with Tissue Rinse Solution A for five and 30 minutes, followed by rinses with Tissue Rinse Solution B for two and five minutes, all at RT. Sections were then quickly rinsed with Tissue Stain Base Solution (- X-Gal Stock solution) for five minutes and then incubated overnight with the Tissue Stain Base Solution (+ X-Gal Stock solution, 1:40 dilution) at 37˚C. X-Gal Stock solution (40mg/mL) was removed from -20˚C storage and warmed at RT prior to mixing to avoid precipitate forming.

EdU (5-ethynyl-2´-deoxyuridine) *in vivo* Labeling

Dams were injected IP with 30 mg/kg body weight of EdU (Invitrogen) 12 hours prior to harvesting at E18.5 (Fig. 4.). Sections were immunostained using the Click-iT kit according to

the manufacturer's protocol (Invitrogen). For co-stains with EdU, the IHC protocol was adapted such that EdU staining was performed before the addition of the secondary antibody.

Microscopy

Histological images were captured using either a Zeiss AxioObserver fluorescence microscope equipped with an Apotome 2 structured illumination device, 20x, 40x oil immersion, and a Hamamatsu Orca Flash v4.0 digital camera or a Zeiss LSM 710 confocal microscope. β-gal and *Mllt11 in situ* staining was captured using an upright Zeiss PrimoStar compound microscope with an ERc5s color camera. Images were processed using Zen software (Zeiss) and figure montages assembled in Photoshop CS6 (Adobe) and Affinity Photo 2.

Image Sampling and Quantification

For analysis of immunostaining markers and EdU labeling, counting frames were randomly placed in respective layers of interest (RL: 50 x 50µm, EGL: 25 x 25µm/25 x 50µm, anchoring centre base: 25 x 50µm, molecular layer or ML: 75 x 75µm, granular layer or GL: 75 x 75µm, cardinal lobes: 100 x 100µm) using ImageJ (FIJI; Schindelin et al., 2012). Anywhere from one to eight counting frames were analyzed per histological section, with at least three histological sections of the cerebellum taken from three to five different animals for each strain. Pax6+ and EdU+ cell counts were performed in entire folia which was partitioned by drawing a straight line between the base of adjacent fissures that make up a single lobe. The "directionality" plugin in FIJI was used to analyse dispersion and orientation of Nestin+ Bergmann glia (BG) fibers at anchoring centres. The analysis frame (40 x 40µm) was placed with the upper margin along the midline of the fissure and lateral margin at the base of the

fissure along the outer EGL boundary. For directionality analyses, the 'direction (°)' value reports the center of the gaussian distribution, and the 'dispersion (°)' value reports the standard deviation of the gaussian. The "selection brush tool" in ImageJ was used to outline the entire cerebellum, EGL, and first 100µm of the RL and the area calculated. The "straight" tool in ImageJ was used to measure EGL thickness, GL thickness, ML thickness, fissure depth, and folia height. To measure folia heights, a straight line was drawn from the base of adjacent fissures parallel to the EGL surface. At the midpoint, a perpendicular line was drawn out to the crown of the folia (including the EGL) and a length measurement was taken. To measure fissure depths, a straight line was drawn across the crowns of adjacent folia. Along the line (at the fissure point), the "straight" tool was used to measure the depth to the base of the fissure (inner EGL boundary).

At least 3 axial levels were analyzed per animal. To ensure consistency among samples, cell counts were restricted to images taken from approximately the same axial regions, identified by continuity with the midbrain and ventricular space between the brainstem anteriorly.

Statistical Analysis

GraphPad Prism V9 software was used to perform all statistical analyses and to produce graphical representations of the data. Statistical differences were determined with Student's t-tests (two-tailed) with Welch's correction. In all statistical analyses, a minimum of three control and three cKO animals were used for quantifications using the unbiased and systematic sampling method described previously (Yamada et al., 2014). Bar and line charts were constructed using GraphPad Prism V9 software (Massachusetts, USA), with results shown as mean ± standard deviation (SD) and each point representing an individual (averaged over three serial images). In

all quantification studies, significance level was set at $P \leq .05$ (*$P \leq .05$, **$P \leq .01$, ***$P \leq .001$, ****$P \leq .0001$).

RESULTS

Mllt11 Expression Pattern in the Embryonic Cerebellum.

Previous studies have described *Mllt11* expression in post-mitotic neurons throughout the developing CNS, but its expression in the developing cerebellum remains uncharacterized (Yamada et al., 2014). To determine if *Mllt11* is expressed during mouse cerebellar development, we used the targeted *Mllt11* allele, which includes a *lacZ* gene inserted into the locus. We observed β-galactosidase (β-gal) staining in the rhombic lip region from E12.5 to E18.5 (Fig.4A-E). At E12.5, β-gal staining was observed throughout the dorsal half of the cerebellar primordium (Fig. 4A), showing a spatial expression pattern resembling the subpial stream of rostrally-migrating Deep Cerebellar Nuclei (DCN) as they move into the Nuclear Transitory Zone (NTZ; (Fink et al., 2006)). GCPs do not leave the RL until around E13 (Consalez et al., 2020). By E14.5, β-gal staining became more widespread across the entire cerebellum primordium, including the developing EGL (Fig. 4B). At this stage, GCPs rapidly emerge from the RL, migrate tangentially to cover the dorsal surface of the primordium, and form the EGL by E15.5. At E16.5, β-gal staining intensity increased compared to previous stages and exhibited a similarly widespread distribution throughout the entire cerebellum, including the RL and faintly in the EGL (Fig. 4C). At this stage, GCs continue their tangential migration along the dorsal surface of the cerebellar primordium, with some undergoing radial migration. These radially migrating GCs move inward along Bergmann glial (BG) fibers to populate the cerebellar core in a diffuse manner (Chung, Kim, Jung, Lee, & Jeong, 2010). It is important to note that

these can be considered "early" inwardly migrating GCs, as the majority of radial migration occurs after birth (Chung et al., 2010). At E18.5, *Mllt11* locus activity, identified by β-gal staining, was widespread throughout the entire cerebellum, including the RL and EGL in both lateral (Fig. 4D) and medial sections (Fig. 5E). At this time point, GCs undergo clonal expansion in the EGL, and some postmitotic GCs migrate inward after a switch to radial migration (Chung et al., 2010; Consalez et al., 2020).

To validate the accuracy of β-gal staining in reflecting *Mllt11* gene expression, we conducted ISH on E18.5 cerebella to examine the distribution of *Mllt11* transcripts. The results showed a similarly diffuse distribution of *Mllt11* mRNA throughout the cerebellum, including the RL and EGL (Fig. 5F). Overall, the spatiotemporal expression pattern of *Mllt11* is consistent with the migration of cells in the developing cerebellum, including GCs.

Conditional Knockout of *Mllt11* in Migrating Granule Cells

The expression pattern of *Mllt11* in the developing RL, EGL, and GL suggested its potential involvement in the migration of GCs (Consalez et al., 2020). To investigate the role of *Mllt11* in cerebellar development, we employed a loss-of-function approach by inactivating *Mllt11* using the $Cux2^{CreERT2}$ driver, which is specific to the excitatory derivatives of the RL (GCs and UBCs) while leaving the VZ derivatives largely unaffected (Capaldo & Iulianella, 2016; Iulianella, Wingate, Moens, & Capaldo, 2019). The tamoxifen-inducible $Cux2^{CreERT2}$ driver provided temporal control over *Mllt11* excision, allowing for the analysis of each GC-specific developmental process (Fig. 3). To visualize mutant cells, $Cux2^{CreERT2}; Mllt11^{flox/+}$ mice were crossed with the *Ai9 TdTomato* fluorescent reporter transgene, allowing for TdTomato fluorescence in cKO cells. Analyses were performed at E18.5 when the cerebellar surface has

undergone morphological changes, including the formation of the four principal fissures (Preculminate (Pc), Primary (Pr), Secondary (Sec), and Posterolateral (Pl)) that separate the five cardinal lobes (Anterobasal (Ab), Anterodorsal (Ad), central, posterior, and inferior). The development of fissures and subsequent folia growth relies on coordinated "anchoring centres" at the base of each fissure, which orchestrate GC proliferation and inward migration along fibres from BG. During cerebellar development, *Cux2* activity is restricted to the RL, and Cux2+ cells are fate-restricted to become mature GCs (Capaldo & Iulianella, 2016). Thus, the *Cux2*$^{CreERT2/+}$ line would be an ideal genetic strategy to take out Mllt11 in the highly migratory GC population. To capture granule cell precursors (GCPs) as they leave the RL, form the external granular layer (EGL), and begin to migrate into the core, tamoxifen was administered at E12.5 (Fig. 3). Cre-mediated excision of *Mllt11* at this time point allowed for investigation of its role in both tangentially migrating GCPs as they form the EGL (Fig. 3A) and in early-inwardly migrating GCs (Fig. 3B). Cre activity was confirmed through TdTomato fluorescence in the RL, EGL, and some cells within the core of E18.5 cerebella (Fig. 5A-B, A'-B'), consistent with previous work using this genetic strategy (Capaldo & Iulianella, 2016). To confirm the identity of tdTomato-labeled cells, we stained for cell-type specific markers: Pax6 for GC, Calbindin for Purkinje cells (PC), and Pax2 for inhibitory interneurons (IN). Almost all tdTomato-labeled cells were Pax6^{+} GCs (Fig. 6A-B, D-E) in both the RL (Fig. 6B', D', E') and core (Fig. 6B'', D'', E'') regions of the cerebellum. No tdTomato+ cells expressed Pax2 (Fig. 6F-H), and only a few, if any, were surrounded by Calbindin cytoplasmic stain (Fig. 6I-K). At this stage, PCs form the diffuse Purkinge Plate (PP) before progressively settling into a monolayer after birth. TdTomato-labeled cells found within this PC layer likely correspond to GCs at other axial levels that migrated over,

under, or between PCs, as there was minimal overlap between TdTomato fluorescence and Calbindin staining in most cells (Fig. 6 I-K).

During Embryonic Cerebellar Development, *Mllt11* Loss Resulted in Smaller Cerebella, Shallower Principal Fissures, Smaller Folia, and Enlarged Rhombic Lips

To assess any gross morphological impacts of *Mllt11* loss on the cerebellum, cerebellar size, folia development, fissure formation, expansion of the EGL, and morphology of the RL were examined. All these processes rely on the proper genesis, migration, and maturation of GCs. Gross evaluation of *Mllt11* cKOs at E18.5 revealed smaller cerebella with significantly reduced foliation compared with controls (Fig. 7A-B). Total cerebellar area was significantly decreased in *Mllt11* mutants (Fig. 7A-B, C; $P = 0.002$, N = 5), accompanied by a reduction in EGL areas (Fig. 7A-B, C; $P = 0.002$, N = 5). When expressed as a ratio (EGL to total cerebellar area), there was no difference between genotypes (Fig. 7C; $P = 0.653$, N = 5), indicating a proportional reduction in EGL size relative to the decrease in total cerebellar area observed in *Mllt11* cKOs.

Mllt11 cKOs exhibited shallower depths of both the Pc (Fig.7A'', B''; $P = 0.0002$, N = 5) and Pr (Fig. 7A''', B'''; $P = 0.006$, N = 5) fissures compared with controls. Although statistical analysis of the Sec fissure did not reach significance (Fig. 7A, B; $P = 0.125$, N = 5), *Mllt11* mutants still displayed a noticeable reduction in its depth. In conjunction with the shorter fissures, *Mllt11* cKOs exhibited shorter Ab (Fig. 7A-B; $P = 0.0004$, N = 5) and Ad (Fig. 7A', B'; $P = 0.002$, N =5) cardinal lobes. The average width of the EGL did not differ markedly between *Mllt11* cKOs and controls at the crown of either lobe, while folia height, which included the EGL in measurements, were significantly shorter in cKOs (Fig. 7E). During foliation, anchoring

centres at the base of each fissure remain relatively fixed while folia grow outward. All four principal fissures formed in *Mllt11* cKOs, they were significantly shallower compared to controls (Fig. 7), indicating potential disruptions in folia lengthening once anchoring centres had been established. Folia lengthening is a complex process driven by self-sustaining proliferation of GCPs and their directed inward migration by BG fibers (Sudarov & Joyner, 2007). Either of these processes may be affected by the loss of *Mllt11*. Furthermore, the size and shape of folia primarily depend on the timing and positioning of anchoring centres formation. Hence, the reduced folia size in *Mllt11* mutants may reflect a developmental delay in anchoring centre formation (Sudarov & Joyner, 2007).

Interestingly, *Mllt11* cKO cerebella also exhibited enlarged RLs relative to controls (Fig. 7F-G, H; $P = 0.006$, N = 5). The RL region is densely packed with GCPs that have yet to migrate tangentially to form the EGL. At E18.5, an enlarged RL region can imply various possibilities. However, considering the role of Mllt11 in neocortical and retinal neuron migration, the most logical explanation is a defect in tangential migration, with *Mllt11* loss resulting in GCPs unable to translocate successfully from the RL at the same rate as controls (Blommers, Stanton-Turcotte, & Iulianella, 2023; Stanton-Turcotte et al., 2022). The resulting migration defect is reflected in an enlargement of the RL due to the aberrant accumulation of precursors (Fig. 7I-K).

Mllt11 **Loss Disrupted Bergmann Glia Fibers at Anchoring Centres**

To elucidate a potential mechanism underlying foliation defects in *Mllt11* mutants, we set out to investigate the integrity of anchoring centres. The establishment of functional anchoring centres at the base of each fissure is a crucial event in driving foliation. Genetic alterations can delay the onset and alter the position of anchor points, ultimately leading to disruptions in

surface morphogenesis (Lejeune, Javili, Weickenmeier, Kuhl, & Linder, 2016; Sudarov & Joyner, 2007). While multiple factors contribute to the formation of functional centres, a critical step to their cytoarchitecture is the reorganization of BG fibers into a fan shape at the base of each fissure by E18.5 (Sudarov & Joyner, 2007). As the cerebellar surface undergoes foliation, BG fibers surrounding the base of each fissure undergo a change in orientation: instead of running parallel, they begin to radiate towards the invaginating pial surface of the anchoring centre (Fig. 8E) (Sudarov & Joyner, 2007). The mechanism underlying this shift in BG fibers is not well understood, and it is unclear whether the reorganization is an active process intrinsic to the glia or a passive mechanical consequence of fissure formation (Sudarov & Joyner, 2007). Given that BG fibers serve as tracks for inward migration of GCs, their orientation is crucial and likely contributes to proper migration.

To visualize BG fibers, I utilized Nestin, a type IV intermediate filament protein that is expressed by multipotent neural stem cells and radial (Bergmann) glia in the cerebellum (Li et al., 2013). As expected, Nestin staining revealed atypical fanning patterns at anchoring centres in *Mllt11* cKOs relative to controls (Fig. 8A-D). At the base of the Pc fissure, *Mllt11* cKOs exhibited BG fibers oriented in parallel without proper radiating patterns towards the base (Fig. 8B, D). In contrast, control cerebella displayed the typical fanning pattern with fibers radiating towards the base of the fissure (Fig. 8A, C). Quantitative analysis of BG fiber directionality at the Pc fissure revealed a reduction in fiber dispersion (Fig. 8F; $P = 0.004$, N = 4) and average angle (direction; Fig. 8F; $P = 0.0009$ N = 4) in *Mllt11* cKOs relative to controls. Analysis at the Pr fissure showed a non-significant reduction in dispersion (Fig. 8F; $P = 0.466$, N = 4) and average angle (direction; Fig. 8F; $P = 0.055$, N = 4). Our current understanding of the mechanisms underlying cerebellar foliation remains incomplete, making it challenging to

interpret this result as either an active mechanism responsible for the foliation defect in *Mllt11* cKOs or a mechanical consequence of another process occurring at the anchoring centre, such as reduced inward migration of GCs.

Mllt11 Loss Resulted in Fewer Pax6$^+$ Cells at Anchoring Centres and Populating Dorsal Lobes

GCs are another critical component to functional anchoring centres in the developing cerebellum. The first manifestation of anchoring centre formation involves a burst in GC proliferation, resulting in thickening and invagination of the EGL (Sudarov & Joyner, 2007). Within the invaginated region of the EGL, GC differentiation rates increase, and by E18.5, some postmitotic GCs begin to migrate inward along BG fibers, which serve as a scaffold (Sudarov & Joyner, 2007). GCs also rely on intrinsic programs to regulate their migration. For instance, morphological changes mediated by the cytoskeleton are necessary for GCs to establish proper contact with BG scaffolding and initiate glial-guided migration (Rahimi-Balaei et al., 2018). Therefore, any disruption to GCs, including their intrinsic migratory ability or to the integrity of their migratory substrate (BG fibers), is likely to affect their translocation from the EGL and subsequently alter anchoring centre cytoarchitecture and foliation. In addition to BG disruption, it was also anticipated that *Mllt11* loss would alter the intrinsic migration program of GCs through potential dysregulation of the cytoskeleton, hindering their ability to migrate inward from the EGL.

Pax6 serves as a marker for GCs (Engelkamp, Rashbass, Seawright, & van Heyningen, 1999; Englund et al., 2006), and is maintained in GC precursors throughout their maturation process, from the RL at birth to their final position in the GL (Stoykova & Gruss, 1994). At

E18.5, Pax6 robustly labeled GCs and their precursors throughout the developing cerebellum, including the EGL and core (Fig. 9A-B, F-G). To investigate inward (radial) migration, we compared two distinct populations of GCs: 1) GCs that had successfully migrated inward from the EGL and were now located within the folia, and 2) GCs that were in the process of inward migration, adjacent to anchoring centres (Fig. 9I). we found that Pax6 staining revealed fewer GCs successfully migrated inward from the EGL in *Mllt11* mutant cerebella compared to controls (Fig. 9A-B, F-G, F'-G'). At E18.5, there was a significant reduction in the number of Pax6$^+$ cells within both the Ab (Fig. 9C; $P = 0.01$, N = 5) and Ad (Fig. 9C; $P = 0.02$, N = 5) lobes in *Mllt11* cKOs relative to controls (Fig. 9F', G'). This finding suggested that the loss of *Mllt11* likely affected GC migration, resulting in underdeveloped folia with smaller areas (Fig. 9F'-G'). Normalizing Pax6 counts to account for the smaller folia area revealed no significant differences in the Ab (Fig. 9C; $P = 0.203$, N = 5) and Ad (Fig. 9C; $P = 0.85$ N = 5) lobes between genotypes. However, these non-significant results following normalization should not be interpreted as a negative result. Rather, the reduced population of GCs in the dorsal lobes explains why *Mllt11* cKOs exhibited smaller and less developed folia. Considering that folia lengthening is an active process driven by self-sustaining proliferation and inward migration of GCs, *Mllt11* loss may disrupt the population of GCs successfully populating dorsal lobes, hindering their outward growth. Further examination of inward migration at anchoring centres revealed reduced Pax6$^+$ cell counts just inside the Pc (Fig. 9H; $P = 0.03$, N = 5) and Pr (Fig. 9H; $P = 0.003$, N = 5) fissures in *Mllt11* cKOs compared with controls (Fig.9F'-G'). Below these anchoring centres, Pax6$^+$ cells were likely inwardly migrating GCs dependent on the scaffolding provided by underlying BG fibers. Since BG fibers were disrupted at anchoring centres in *Mllt11* cKOs (Fig. 8), the reduced GC counts at the bases of the Pc and Pr fissures (Fig. 9H) may be a

consequence of a disruption in BG glia cytoarchitecture. Alternatively, *Mllt11* loss may disrupt the migratory behaviour of GCs through potential cytoskeletal dysregulation, as proposed in migrating UL CPNs of the cortex (Stanton-Turcotte et al., 2022) and retinal neuroblasts (Blommers et al., 2023). In light of this, examining the anchoring centres as sites of inward migration revealed a reduction of Pax6+ cells in *Mllt11* cKOs (Fig. 9I), suggesting a radial migration defect.

Mllt11 Loss Leads to Impaired Granule Cell Migration

To further investigate a potential migration defect exhibited by *Mllt11* cKOs, pregnant dams were pulsed with EdU late on E17, and cerebella were analyzed 12 hours later. This time point captured both tangentially migrating GCPs from the RL, occurring from E13-E17.5 (Rahimi-Balaei et al., 2018), and inwardly radially migrating GCs, which begins as early as E14 (Chung et al., 2010). While complete radial migration from terminal division to settlement in the GL has been reported to take an average of 2 days, results described below may suggest a shorter time course, making the 12-hour pulse a viable window to analyze this migration process. The EdU pulse at E17 labeled cells within the RL, EGL, and core of control (Fig. 10A, E, G, K) and cKO cerebella (Fig. 10B, F, H, L). *Mllt11* cKOs exhibited a clear reduction in the number of EdU^+ cells in both the Ad (Fig. 10F, O; $P = 0.0005$, N = 5) and Ab (Fig. 10N, O; $P = 0.0005$, N = 5) lobes compared with controls (Fig. 10E, M). Pax6 co-staining revealed that some EdU^+ cells populating dorsal folia expressed low levels of Pax6, suggesting they were postmitotic GCs that had migrated inward (Fig. 10Q-S, white arrows). This finding contradicts the previous literature suggesting a longer migratory time course for GCs, and it suggests that the migratory dynamics of late embryonic GCs may differ from early postnatal mice studied *in vitro* (Yacubova &

Komuro, 2002). Sudarov and Joyner (2007) also showed that GCs at anchoring centres exhibit a shorter mitotic index which may explain the rapid incorporation of EdU and subsequent migration inward from the EGL (Fig. 10). However, many EdU^+ cells were $Pax6^-$, likely representing a combination of PCs and inhibitory interneurons derived from the VZ (Fig. 10Q-S). Although a longer EdU pulsing experiment (~2 days) capturing more inwardly migrating GCs would have been ideal, the extensive and rapid clonal expansion in the EGL diluted the EdU signal and made it challenging to resolve single cells (data not shown). Overall, this EdU pulsing experiment provided evidence that *Mllt11* loss impacted GC migration, resulting in less foliation and smaller folia (Fig. 10E-F, M-N). Normalizing EdU counts to smaller folia areas masked the difference in the Ad (Fig. 10O; $P = 0.167$, N = 5) and Ab (Fig. 10O; $P = 0.558$, N = 5) lobes between genotypes. The reduced number of EdU^+ cells in the dorsal lobes could explain the smaller and less developed folia observed in *Mllt11* cKOs (Fig. 7), as folia lengthening relies on self-sustaining GC proliferation and inward migration. Overall, these findings suggest that *Mllt11* loss may hinder folia outgrowth at least in part by disrupting inward migration.

An EdU pulse at E17 captured the final wave of tangential migration of GCPs from the RL (Fig. 10G, H, K, L). Since *Mllt11* was expressed in the RL and adjacent EGL at E18.5 (Fig. 10C), and the excision event was restricted to this region (Fig. 10D), this genetic strategy and birth-dating experiment provided an ideal approach to investigate potential tangential migration defect of GCPs emanating from the RL. Since GCPs are born in the RL and migrate rostrally over the dorsal surface of the developing cerebellum, we analyzed the RL and seven sequential regions of the EGL to follow EdU^+ cells along their migratory path (Fig. 10P). In the RL, controls (Fig. 10K') displayed fewer EdU^+ cells compared with cKOs (Fig. 10L'), which was more densely packed with labelled cells (Fig. 10P; $P = 0.005$, N = 5). Moving along sequential

bins, there was a progressive, non-significant trend toward fewer EdU^+ cells in cKOs (Fig. 10K) compared to controls (Fig. 10L). Analysis of the distal-most EGL bin (#8) revealed a significant reduction in EdU^+ cells in cKOs (Fig. 10L'') relative to controls (Fig. 10K'', P; $P = 0.005$, N = 5). Taken together, analysis of the RL and distal EGL suggested a potential tangential migration defect in *Mllt11* cKOs compared with controls. It is important to consider that GCPs are proliferating throughout the EGL at this stage. Therefore, it is possible that *Mllt11* loss led to a reduction in EdU^+ cells in the distal EGL by affecting the proliferation of GCPs during or after their migration. Additionally, it remains unclear whether GCPs divide after completing their migration or if they simultaneously combine migration and proliferation, making it challenging to draw a definitive conclusion regarding a tangential migration defect. However, given the role of Mllt11 in the migration of cortical (Stanton-Turcotte et al., 2022) and retinal (Blommers et al., 2023) neurons, it is likely that Mllt11 plays a similar role in the tangential migration of GCPs in the cerebellum.

Mllt11 Loss Left the Purkinje Cell and Inhibitory Interneuron Populations Largely Unaffected

While the genetic strategy employed for the current study restricted *Mllt11* loss to predominantly GCs, it was important to investigate any possible effects on other cerebellar populations, specifically, PCs and inhibitory interneurons (INs). To visualize PCs, Calbindin D-28K, known for its high expression in PCs (Barski et al., 2003), was used. At late embryonic stages, PCs arrange themselves in a diffuse multilayer PP below the EGL (Sudarov & Joyner, 2007). PCs are essential for anchoring the developing cytoarchitecture of the cerebellum, along with GCs and BG as described above. During early cerebellar morphogenesis, the PP undergoes

inward folding, corresponding to the thickening and invagination of the overlying EGL (Sudarov & Joyner, 2007).

Sudarov and Joyner (2007) proposed that the inward folding of the PP is likely a consequence of the accumulation of migrating GCs. Given the disrupted inward migration of GCs in *Mllt11* cKOs and the subsequent disruption of fissure development, it was expected that the PP might also be affected. At E18.5, Calbindin staining revealed disruptions to the invagination of the PP in *Mllt11* cKOs (Fig. 11A-D), with PCs less clustered in columnar formations in cKOs relative to controsl (Fig. 11D' vs. C'). Although PCs did not accumulate in subcortical regions, and the PP still formed in cKOs, the degree of infolding at dorsal fissures was reduced on the cKOs (Fig. 11C'-D').

To investigate whether *Mllt11* loss in Cux2+ cells in the developing cerebellum, we used Pax2 to visualize GABAergic INs (Weisheit et al., 2006). Inhibitory INs are generated from the VZ around E13 and subsequently delaminate and migrate into the cerebellar parenchyma (Leto et al., 2016). By late embryonic stages, Pax2^{+} INs are distributed throughout the core and developing folia (Grimaldi, Parras, Guillemot, Rossi, & Wassef, 2009). Staining E18.5 cerebella with Pax2 revealed minor distribution differences of INs between controls (Fig, 12A, C) and *Mllt11* cKOs (Fig, 12B, D). Cell counts conducted in each cardinal lobe (Fig.12E) showed no significant differences in Pax2^{+} INs, except in the Ad lobe, where there were more Pax2^{+} cells in cKOs (Fig. 12D) compared with controls (Fig. 12C, F; $P = 0.039$, N = 4). One interpretation of this result is that the foliation defects exhibited by *Mllt11* mutants led to an aberrant accumulation of Pax2^{+} cells in the core of the folia (Fig. 12D), instead of their normal migration into the growing folia (Fig. 12C). No significant differences were detected in the numbers of inhibitory INs in the remaining cardinal lobes (Fig. 12F), suggesting the formation was largely

unaffected by *Mllt11* loss. However, the disrupted foliation of *Mllt11* cKO cerebella likely interfered with their proper distribution of Pax2+ INs within the distal columns of developing lobes (Fig. 12C, D).

DISCUSSION

The experiments conducted herein aimed to investigate the role of Mllt11 in the migration of GCs within the developing mouse cerebellum. This was achieved by characterizing the expression profile of *Mllt11* throughout embryonic and postnatal development and using an inducible knockout model to specifically excise *Mllt11* in excitatory lineages of the cerebellum, including GCs. The expression pattern of β-gal in the targeted *Mllt11* allele confirmed its widespread expression throughout the cerebellum during embryonic development. ISH provided further confirmation of the reported β-gal expression pattern. Therefore, a genetic strategy was employed to conditionally inactivate *Mllt11* specifically within the excitatory lineages of the cerebellar anlage. This was achieved by utilizing the $Cux2^{CreERT2}$ driver to excise *Mllt11* in GCPs originating from the RL during early embryogenesis, as previously described by the Iulianella lab (Capaldo & Iulianella, 2016). This approach revealed a potential role for Mllt11 in the formation of anchoring centres at principal fissures and in the migration of GCs.

In the absence of *Mllt11*, cerebella were smaller and less foliated, exhibiting shallower fissures with disrupted BG fiber patterns at their base. The atypical BG fibers observed in *Mllt11* cKOs likely impaired radial migration at anchoring centres, resulting in fewer GCs populating the developing folia. The foliation defect observed in *Mllt11* mutants shares similarities, albeit to a lesser extent, with the Engrailed 2 (En2) mutant previously described (Sudarov & Joyner,

2007). In *En2*$^{-/-}$ mutants the delay in anchoring centre formation leads to a smooth cerebellar surface at E17.5 instead of the presence of three principal fissures (Sudarov & Joyner, 2007). By birth, all principal fissures have formed except the Sec fissure, which becomes visible at P1 (Sudarov & Joyner, 2007). The altered timing of anchoring centre formation in *En2*$^{-/-}$ mutants during embryogenesis results in a pronounced postnatal phenotype, with a significantly misshapen lobule VIII (Joyner & Martin, 1987; Sudarov & Joyner, 2007). Similar to *Mllt11* mutants, *En2*$^{-/-}$ mutant cerebella are smaller. The delayed formation of the Sec principal fissure in *En2*$^{-/-}$ mutants causes a reduction in fissure depth which is reminiscent to the phenotype exhibited by *Mllt11* mutants (Sudarov & Joyner, 2007). In *En2*$^{-/-}$ mutants, BG fibers also fail to fan out from the delayed anchoring centres until a later time point, similar to the disrupted fiber orientation observed at the anchoring centres of *Mllt11* cKOs in this study.

In addition to affecting anchoring centre formation, *Mllt11* loss also influenced GC migration. GCs migrate out from the RL and EGL through a stepwise process involving saltatory motion (Edmondson & Hatten, 1987). Microtubules and actin are highly enriched in the leading process which propel the cell forward through dynamic reorganization (assembly and disassembly; (Gregory, Edmondson, Hatten, & Mason, 1988; Hatten, 1993; Rivas & Hatten, 1995)). Disruptions to the actin and microtubule cytoskeletons or their associated motor proteins, which play a crucial role in cellular movement, can inhibit GC migration (Bellion, Baudoin, Alvarez, Bornens, & Metin, 2005; Kawauchi & Hoshino, 2008; Trivedi & Solecki, 2011). For instance, pharmacological inhibition of actin polymerization using cytochalasin B is sufficient to inhibit GC migration (Hatten, 1993). Despite the importance of the cytoskeleton in cellular movement, knowledge of its regulators remains incomplete.

Mllt11 has been identified as a novel cytoskeletal interacting protein, interacting with multiple tubulin isoforms and non-muscle Myosins (Stanton-Turcotte et al., 2022). These interactions likely contribute to the coordination and organization of the dynamic cytoskeleton. In the absence of *Mllt11*, GCs accumulated in the RL, indicating a potential tangential migration defect. Additionally, fewer GCs populated the developing folia, which could be attributed to disrupted anchoring centre cytoarchitecture (BG fibers) or other intrinsic GC processes, such as cytoskeletal disruptions. Cytoskeletal disruptions can lead to aberrant GC migration in the developing cerebellum. For example, dystroglycan (DG) of the dystrophin-glycoprotein complex is expressed in BG endfeet and links the extracellular matrix with the intracellular actin cytoskeleton to form glia limitans (Moore et al., 2002). Deletion of DG in mice causes aberrant BG fiber organization, resulting in GC migration defects and ectopic accumulation in the EGL (Nguyen et al., 2013). This example recapitulates that normal cerebellar histogenesis and GC migration is dependent on proper BG scaffolds mediated by the underlying cytoskeleton. Another example to highlight the integral role of the cytoskeleton comes from β-chimaerin (*Chn2*) null mice (Estep, Wong, Wong, Loui, & Riccomagno, 2018). β-chimaerin is a component of the Rho family of GTPase Activating Proteins (RhoGAPS) which is expressed in a small population of late-born premigratory GCs in the EGL and has specific activity toward another family of GTPases which are key modulators of actin filaments (Estep et al., 2018; Yang & Kazanietz, 2007). β-chimaerin deficiency in mice caused a subset of GCs to be arrested in the EGL, where they differentiated and formed ectopic neuronal clusters likely due to cytoskeletal dysregulation (Yang & Kazanietz, 2007). These examples highlight the critical role of the cytoskeleton in GC migration. Therefore, I speculate that tangential and radial migration defects observed in *Mllt11* mutants are likely due to similar cytoskeletal disruptions.

Overall, this study is the first to identify Mllt11 as a key regulator of GC migration and anchoring centre formation in the developing cerebellum. While the mechanism underlying Mllt11 and its interactions remain unclear, these findings provide further support for its role in promoting neuronal migration and contributing to the development of neuronal cytoarchitecture and lamination in structures across the CNS.

ACKNOWLEDGMENTS

We gratefully acknowledge funding from the Canadian Institutes of Health Research (CIHR PJT-388914) and thank Sarah Whitehead for assistance with animal husbandry.

REFERENCES

Ballif, B. A., Arnaud, L., Arthur, W. T., Guris, D., Imamoto, A., & Cooper, J. A. (2004). Activation of a Dab1/CrkL/C3G/Rap1 pathway in Reelin-stimulated neurons. *Curr Biol, 14*(7), 606-610. doi:10.1016/j.cub.2004.03.038

Barski, J. J., Hartmann, J., Rose, C. R., Hoebeek, F., Morl, K., Noll-Hussong, M., . . . Meyer, M. (2003). Calbindin in cerebellar Purkinje cells is a critical determinant of the precision of motor coordination. *J Neurosci, 23*(8), 3469-3477. doi:10.1523/JNEUROSCI.23-08-03469.2003

Bellion, A., Baudoin, J. P., Alvarez, C., Bornens, M., & Metin, C. (2005). Nucleokinesis in tangentially migrating neurons comprises two alternating phases: forward migration of the Golgi/centrosome associated with centrosome splitting and myosin contraction at the rear. *J Neurosci, 25*(24), 5691-5699. doi:10.1523/JNEUROSCI.1030-05.2005

Blommers, M., Stanton-Turcotte, D., & Iulianella, A. (2023). Retinal neuroblast migration and ganglion cell layer organization require the cytoskeletal-interacting protein Mllt11. *Dev Dyn, 252*(2), 305-319. doi:10.1002/dvdy.540

Capaldo, E., & Iulianella, A. (2016). Cux2 serves as a novel lineage marker of granule cell layer neurons from the rhombic lip in mouse and chick embryos. *Dev Dyn, 245*(8), 881-896. doi:10.1002/dvdy.24418

Chedotal, A. (2010). Should I stay or should I go? Becoming a granule cell. *Trends Neurosci, 33*(4), 163-172. doi:10.1016/j.tins.2010.01.004

Chung, S. H., Kim, C. T., Jung, Y. H., Lee, N. S., & Jeong, Y. G. (2010). Early cerebellar granule cell migration in the mouse embryonic development. *Anat Cell Biol, 43*(1), 86-95. doi:10.5115/acb.2010.43.1.86

Consalez, G. G., Goldowitz, D., Casoni, F., & Hawkes, R. (2020). Origins, Development, and Compartmentation of the Granule Cells of the Cerebellum. *Front Neural Circuits, 14*, 611841. doi:10.3389/fncir.2020.611841

Edmondson, J. C., & Hatten, M. E. (1987). Glial-guided granule neuron migration in vitro: a high-resolution time-lapse video microscopic study. *J Neurosci, 7*(6), 1928-1934. doi:10.1523/JNEUROSCI.07-06-01928.1987

Engelkamp, D., Rashbass, P., Seawright, A., & van Heyningen, V. (1999). Role of Pax6 in development of the cerebellar system. *Development, 126*(16), 3585-3596. doi:10.1242/dev.126.16.3585

Englund, C., Kowalczyk, T., Daza, R. A., Dagan, A., Lau, C., Rose, M. F., & Hevner, R. F. (2006). Unipolar brush cells of the cerebellum are produced in the rhombic lip and migrate through developing white matter. *J Neurosci, 26*(36), 9184-9195. doi:10.1523/JNEUROSCI.1610-06.2006

Estep, J. A., Wong, W., Wong, Y. E., Loui, B. M., & Riccomagno, M. M. (2018). The RacGAP beta-Chimaerin is essential for cerebellar granule cell migration. *Sci Rep, 8*(1), 680. doi:10.1038/s41598-017-19116-w

Evsyukova, I., Plestant, C., & Anton, E. S. (2013). Integrative mechanisms of oriented neuronal migration in the developing brain. *Annu Rev Cell Dev Biol, 29*, 299-353. doi:10.1146/annurev-cellbio-101512-122400

Fink, A. J., Englund, C., Daza, R. A., Pham, D., Lau, C., Nivison, M., . . . Hevner, R. F. (2006). Development of the deep cerebellar nuclei: transcription factors and cell migration from the rhombic lip. *J Neurosci, 26*(11), 3066-3076. doi:10.1523/JNEUROSCI.5203-05.2006

Gregory, W. A., Edmondson, J. C., Hatten, M. E., & Mason, C. A. (1988). Cytology and neuron-glial apposition of migrating cerebellar granule cells in vitro. *J Neurosci, 8*(5), 1728-1738. doi:10.1523/JNEUROSCI.08-05-01728.1988

Grimaldi, P., Parras, C., Guillemot, F., Rossi, F., & Wassef, M. (2009). Origins and control of the differentiation of inhibitory interneurons and glia in the cerebellum. *Dev Biol, 328*(2), 422-433. doi:10.1016/j.ydbio.2009.02.008

Guy, J., & Staiger, J. F. (2017). The Functioning of a Cortex without Layers. *Front Neuroanat, 11*, 54. doi:10.3389/fnana.2017.00054

Hatten, M. E. (1993). The role of migration in central nervous system neuronal development. *Curr Opin Neurobiol, 3*(1), 38-44. doi:10.1016/0959-4388(93)90033-u

Huang, G. J., Edwards, A., Tsai, C. Y., Lee, Y. S., Peng, L., Era, T., . . . Flint, J. (2014). Ectopic cerebellar cell migration causes maldevelopment of Purkinje cells and abnormal motor behaviour in Cxcr4 null mice. *PLoS One, 9*(2), e86471. doi:10.1371/journal.pone.0086471

Iulianella, A., Wingate, R. J., Moens, C. B., & Capaldo, E. (2019). The generation of granule cells during the development and evolution of the cerebellum. *Dev Dyn, 248*(7), 506-513. doi:10.1002/dvdy.64

Joyner, A. L., & Martin, G. R. (1987). En-1 and En-2, two mouse genes with sequence homology to the Drosophila engrailed gene: expression during embryogenesis. *Genes Dev, 1*(1), 29-38. doi:10.1101/gad.1.1.29

Kawauchi, T., & Hoshino, M. (2008). Molecular pathways regulating cytoskeletal organization and morphological changes in migrating neurons. *Dev Neurosci, 30*(1-3), 36-46. doi:10.1159/000109850

Kim, C. H., Oh, S. H., Lee, J. H., Chang, S. O., Kim, J., & Kim, S. J. (2012). Lobule-specific membrane excitability of cerebellar Purkinje cells. *J Physiol, 590*(2), 273-288. doi:10.1113/jphysiol.2011.221846

Lejeune, E., Javili, A., Weickenmeier, J., Kuhl, E., & Linder, C. (2016). Tri-layer wrinkling as a mechanism for anchoring center initiation in the developing cerebellum. *Soft Matter, 12*(25), 5613-5620. doi:10.1039/c6sm00526h

Leto, K., Arancillo, M., Becker, E. B., Buffo, A., Chiang, C., Ding, B., . . . Hawkes, R. (2016). Consensus Paper: Cerebellar Development. *Cerebellum, 15*(6), 789-828. doi:10.1007/s12311-015-0724-2

Li, P., Du, F., Yuelling, L. W., Lin, T., Muradimova, R. E., Tricarico, R., . . . Yang, Z. J. (2013). A population of Nestin-expressing progenitors in the cerebellum exhibits increased tumorigenicity. *Nat Neurosci, 16*(12), 1737-1744. doi:10.1038/nn.3553

Liu, J. S. (2011). Molecular genetics of neuronal migration disorders. *Curr Neurol Neurosci Rep, 11*(2), 171-178. doi:10.1007/s11910-010-0176-5

Marin, O., Valiente, M., Ge, X., & Tsai, L. H. (2010). Guiding neuronal cell migrations. *Cold Spring Harb Perspect Biol, 2*(2), a001834. doi:10.1101/cshperspect.a001834

Metin, C., Vallee, R. B., Rakic, P., & Bhide, P. G. (2008). Modes and mishaps of neuronal migration in the mammalian brain. *J Neurosci, 28*(46), 11746-11752. doi:10.1523/JNEUROSCI.3860-08.2008

Miale, I. L., & Sidman, R. L. (1961). An autoradiographic analysis of histogenesis in the mouse cerebellum. *Exp Neurol, 4*, 277-296. doi:10.1016/0014-4886(61)90055-3

Moffat, J. J., Ka, M., Jung, E. M., & Kim, W. Y. (2015). Genes and brain malformations associated with abnormal neuron positioning. *Mol Brain, 8*(1), 72. doi:10.1186/s13041-015-0164-4

Moore, S. A., Saito, F., Chen, J., Michele, D. E., Henry, M. D., Messing, A., . . . Campbell, K. P. (2002). Deletion of brain dystroglycan recapitulates aspects of congenital muscular dystrophy. *Nature, 418*(6896), 422-425. doi:10.1038/nature00838

Nguyen, H., Ostendorf, A. P., Satz, J. S., Westra, S., Ross-Barta, S. E., Campbell, K. P., & Moore, S. A. (2013). Glial scaffold required for cerebellar granule cell migration is dependent on dystroglycan function as a receptor for basement membrane proteins. *Acta Neuropathol Commun, 1*, 58. doi:10.1186/2051-5960-1-58

Rahimi-Balaei, M., Bergen, H., Kong, J., & Marzban, H. (2018). Neuronal Migration During Development of the Cerebellum. *Front Cell Neurosci, 12*, 484. doi:10.3389/fncel.2018.00484

Rivas, R. J., & Hatten, M. E. (1995). Motility and cytoskeletal organization of migrating cerebellar granule neurons. *J Neurosci, 15*(2), 981-989. doi:10.1523/JNEUROSCI.15-02-00981.1995

Stanton-Turcotte, D., Hsu, K., Moore, S. A., Yamada, M., Fawcett, J. P., & Iulianella, A. (2022). Mllt11 Regulates Migration and Neurite Outgrowth of Cortical Projection Neurons during Development. *J Neurosci, 42*(19), 3931-3948. doi:10.1523/JNEUROSCI.0124-22.2022

Stouffer, M. A., Golden, J. A., & Francis, F. (2016). Neuronal migration disorders: Focus on the cytoskeleton and epilepsy. *Neurobiol Dis, 92*(Pt A), 18-45. doi:10.1016/j.nbd.2015.08.003

Stoykova, A., & Gruss, P. (1994). Roles of Pax-genes in developing and adult brain as suggested by expression patterns. *J Neurosci, 14*(3 Pt 2), 1395-1412. doi:10.1523/JNEUROSCI.14-03-01395.1994

Sudarov, A., & Joyner, A. L. (2007). Cerebellum morphogenesis: the foliation pattern is orchestrated by multi-cellular anchoring centers. *Neural Dev, 2*, 26. doi:10.1186/1749-8104-2-26

Tran, T. S., Kolodkin, A. L., & Bharadwaj, R. (2007). Semaphorin regulation of cellular morphology. *Annu Rev Cell Dev Biol, 23*, 263-292. doi:10.1146/annurev.cellbio.22.010605.093554

Trivedi, N., & Solecki, D. J. (2011). Neuronal migration illuminated: a look under the hood of the living neuron. *Cell Adh Migr, 5*(1), 42-47. doi:10.4161/cam.5.1.13609

Tse, W., Zhu, W., Chen, H. S., & Cohen, A. (1995). A novel gene, AF1q, fused to MLL in t(1;11) (q21;q23), is specifically expressed in leukemic and immature hematopoietic cells. *Blood, 85*(3), 650-656. Retrieved from https://www.ncbi.nlm.nih.gov/pubmed/7833468

Valiente, M., & Marin, O. (2010). Neuronal migration mechanisms in development and disease. *Curr Opin Neurobiol, 20*(1), 68-78. doi:10.1016/j.conb.2009.12.003

Weisheit, G., Gliem, M., Endl, E., Pfeffer, P. L., Busslinger, M., & Schilling, K. (2006). Postnatal development of the murine cerebellar cortex: formation and early dispersal of basket, stellate and Golgi neurons. *Eur J Neurosci, 24*(2), 466-478. doi:10.1111/j.1460-9568.2006.04915.x

Welker, W. I. (1990). The significance of foliation and fissuration of cerebellar cortex. The cerebellar folium as a fundamental unit of sensorimotor integration. *Arch Ital Biol, 128*(2-4), 87-109. Retrieved from https://www.ncbi.nlm.nih.gov/pubmed/2268185

Yacubova, E., & Komuro, H. (2002). Intrinsic program for migration of cerebellar granule cells in vitro. *J Neurosci, 22*(14), 5966-5981. doi:10.1523/JNEUROSCI.22-14-05966.2002

Yamada, M., Clark, J., & Iulianella, A. (2014). MLLT11/AF1q is differentially expressed in maturing neurons during development. *Gene Expr Patterns, 15*(2), 80-87. doi:10.1016/j.gep.2014.05.001

Yang, C., & Kazanietz, M. G. (2007). Chimaerins: GAPs that bridge diacylglycerol signalling and the small G-protein Rac. *Biochem J, 403*(1), 1-12. doi:10.1042/BJ20061750

FIGURE LEGENDS

Figure 1. The two different modes of granule cell migration during embryonic cerebellar development. The first GCPs are born in the RL around E12 and migrate tangentially over the dorsal surface of the cerebellar anlage to form the EGL as depicted in the top schematic at E14.5. Earliest born GCPs preferentially colonize the rostral EGL. The EGL serves as a transient secondary germinal zone in which GCPs undergo extensive clonal expansion. Following a terminal division, postmitotic GCs move into the inner EGL and emit an axon at each pole in the medial-lateral direction which will become parallel fibers. GCs will undergo nuclear translocation along one parallel fiber before extending a radial process and descending along Bergmann glia fibers into the cerebellar core indicative of a switch to radial migration which is depicted in the bottom schematic at E18.5. a, anterior; c, caudal; d, dorsal; p, posterior; r, rostral; v, ventral.

Figure 2. An overview of cerebellar development. (A-B) Schematic illustrations of cerebellar development including posterior views and insets with parasagittal cross-sections at E12.5 (A) and E18.5 (B). At E12.5 the cerebellar primordium surface is smooth. By E18.5, four invaginations, or principal fissures, can be identified on its surface which separate as five cardinal lobes. BS, brainstem; c, caudal; CbP, cerebellar primordium; Cb, cerebellum; d, dorsal; EGL, external granular layer; Mb, midbrain; RL, rhombic lip; r, rostral; v, ventral; VZ, ventricular zone.

Figure 3. Schematic depicting the genesis of cerebellar neurons over experimental timeline. Deep cerebellar nuclei are the first-born cell type around E10, followed by PCs. The first GC precursors are born in the RL around E12. GCs undergo (A) tangential migration to form the EGL and (B) early inward migration into the cerebellar core during embryonic periods of cerebellar development. Tamoxifen (TAM, red triangle) was administered at E12.5 to induce recombination in GCs as they leave the RL and undergo the two migratory processes depicted in (A, B). EdU (green triangle) would also be injected 12 hours prior to harvesting. (1) Mouse embryo with corresponding sagittal brain sections to highlight cerebellar morphology. DCN, deep cerebellar nuclei; EdU, 5-Ethynyl-2'-deoxyuridine; GCs, granule cells; INs, interneurons; PCs, Purkinje cells; TAM, Tamoxifen.

Figure 4. *Mllt11* expression profile in the developing cerebellum. (A-F) Sagittal sections taken of the targeted *Mllt11* locus (with inserted *lacZ* cDNA), visualized using β–gal staining, and *Mllt11* mRNA by ISH. Schematics in upper right corner of panels depict approximate medial-lateral position of the section. (A) At E12.5, β-gal staining was widespread throughout the dorsal half of the CbP and faintly in the RL. (B) At E14.5, β–gal staining was more widespread through the entire primordium including the EGL. (C) At E16.5 β–gal staining was intense throughout the core and faintly detected in the RL and EGL. Lateral (D) and medial (E) sections at E18.5 show β–gal staining throughout the core, EGL, and RL. (F) *Mllt11* expression in the cerebellum at E18.5 revealed a similar expression pattern to β–gal staining. Scale bar: 100μm for all panels (A-F). a, anterior; CbP, cerebellar primordium; Cb, cerebellum; ChP, choroid plexus; d, dorsal; EGL, external granular layer; Mb, midbrain; p, posterior; RL, rhombic lip; v, ventral; VZ, ventricular zone.

Figure 5. Sample images of TdTomato fluorescence in recombined cells of the developing cerebellum following Tamoxifen induction of *Cux2^{CreERT2}; Ai9* brains. (A-B) E18.5 parasagittal cerebellum induced at E12.5 co-stained with DAPI over TdTomato. Tomato labeling was restricted to cells of the RL, EGL, and some cells in the core. (A'-B') Higher magnification view of the RL region of corresponding panels (A-B). Scale bar: 100µm for all panels (A-B'). a, anterior; ChP, choroid plexus; d, dorsal; EGL, external granular layer; Mb, midbrain; p, posterior; RL, rhombic lip; v, ventral.

Figure 6. Inducing *Cux2^{CreERT2}*-driven recombination at E12.5 almost exclusively labeled granule cells. (A-B, D-E) Parasagittal section of an E18.5 cerebellum induced at E12.5 exhibited tomato-labeled cells which almost exclusively expressed the GC marker, Pax6. Yellow and purple insets in (E) correspond to colour-coordinated borders of panels (B', D', E', B'', D'', E''). (B', D', E') Almost all Tomato labeled cells of the RL and adjacent EGL region were Pax6^{+}. (B'', D'', E'') Almost all Tomato-labeled cells in the core expressed Pax6 except a few which were Pax6^{-} (fuchsia arrow). (C) Markers for cerebellar cell types of interest. (F-H) Tomato labeled cells in the core of the cerebellum did not express the inhibitory IN marker, Pax2 (yellow arrows). (I-K) Sample image taken from the posterior lobe revealed that almost all Tomato-labeled cells did not express the PC marker, Calbindin. Most Tomato-labeled cells seen throughout the Calbindin^{+} PP were likely inwardly migrating GCs moving over, beneath, and between the PCs. Very few (if any) cytoplasmic Calbindin+ stain surrounded Tomato-labeled cells in this layer. Scale bar: 50µm for (A-K). a, anterior; d, dorsal; Cb, cerebellum; EGL, external granular layer; p, posterior; RL, rhombic lip; v, ventral.

Figure 7. *Mllt11* loss resulted in smaller cerebella with shallower principal fissures, smaller folia, and enlarged rhombic lips. (A, B) Parasagittal sections of E18.5 cerebella stained with DAPI revealed controls (A) with larger cerebellar and EGL areas compared to *Mllt11* mutants (B). (A, B) At E18.5 the four principal fissures and five cardinal lobes are present in both controls (A) and mutants (B): Ab (white outline), Ad (red outline), central (green outline), posterior (yellow outline), and inferior (pink outline). (C) Bar chart comparisons of total cerebellar area, EGL area, and respective ratios for controls versus *Mllt11* cKOs. (A') Ad lobes were taller in controls compared to *Mllt11* cKOs (B'). Pc (A'', B'') and Pr (A''', B''') fissure depths were also deeper in controls (A'', A''') compared to *Mllt11* cKO mutants (B'', B'''). Coloured outlines in (A'-A''', B'-B''', F, G) correspond with insets in underlying panels. (D) Bar chart comparisons of three principal fissure (Pc, Pr, and Sec) depths, dorsal folia (Ab and Ad) heights, and I average EGL widths in controls versus *Mllt11* cKOs. (F) Control RLs were smaller than *Mllt11* cKOs (G). (H) Schematic of how RL areas were calculated (first 100 μm) with a bar chart comparison of RL areas of controls versus *Mllt11* mutants. (I, J) Schematic EGL tracings in control (I) and cKO (J) cerebella with inset boxes colour-coordinated to outlines around corresponding panels above. (K) Schematic summary of control versus *Mllt11* cKO comparing folia height, fissure depth, and RL size. Welch's *t*-test, (A, B, F, G) N = 5. Data presented as mean ± Sd. n.s., not significant. **$P \leq 0.01$; ***$P \leq 0.001$. Scale bar: 100µm for (A, B), 50µm for (A'-A''', B'-B'''), and 25µm for (F, G). a, anterior; Ab, anterobasal; Ad,

anterodorsal; ChP, choroid plexus; d, dorsal; EGL, external granular layer; Mb, midbrain; p, posterior; pc, preculminate; pl, posterolateral; pr, primary; RL, rhombic lip; sec, secondary; v, ventral.

Figure 8. *Mllt11* loss resulted in disrupted Bergmann glia fibers at anchoring centres. (A-D) Sagittal sections of E18.5 control (A, C) and *Mllt11* cKO (B, D) cerebella at the Pc fissure stained with Nestin to visualize BG fibers. (A) Controls exhibited a typical fanning pattern of BG while cKOs (B) had atypical fibers running in parallel. (E) Schematic depicting an "anchoring centre" which forms at the base of each fissure and coincides with increased GC proliferation, EGL thickening, invagination of the underlying PCL, and BG fibers that radiate toward the base of the fissure creating a fanning pattern. (F) Bar graph comparisons of average direction (°) and dispersion (°) angle of fibers in a 40 x 40 μm bin placed at the base of each fissure with the upper margin of the bin aligning with the midline of the fissure. Controls exhibited typical fanning pattern of BG fibers at anchoring centres with a greater average angle (direction) and degree of dispersion at the Pc fissure. *Mllt11* cKOs exhibited atypical fiber orientations with smaller average fiber angles (direction) and degrees of dispersion at the Pc but not the Pr fissure. Welch's *t*-test, (A, B) N = 4. Data presented as mean ± SD. n.s., not significant; **P ≤ 0.01; ****P ≤ 0.0001. Scale bar: 20µm for (A-D). Pc, preculminate; Pr, primary.

Figure 9. Loss of *Mllt11* disrupted early inward migration of granule cells in the embryonic cerebellum. (A-B, D-E, F-G) Medial sagittal sections of E18.5 cerebella stained with Pax6 with images capturing the dorsal cardinal lobes (Ab and Ad) and cerebellar core. (A, D, F) Control cerebella exhibited larger folia and deeper fissures, while *Mllt11* cKOs (B, E, G) were shorter with shallower fissures. High-magnification views of the Ad lobe revealed fewer GCs populating the lobe in *Mllt11* cKOs (G') compared to controls (F'). At each anchoring centre below the $Pax6^+$ EGL at the base of the fissure, controls (F') had more inwardly migrating GCs compared to cKOs (G'). I Bar chart comparisons of control versus cKO total $Pax6^+$ cell counts in Ab and Ad lobes with corresponding normalized counts per 5000 μm^2 area. (H) Bar char comparison of control versus cKO $Pax6^+$ cell counts in 25 x 50 μm bins placed at the base of the Pc and Pr fissures just inside the EGL. (I) Schematic of the Ad lobe to illustrate how the two $Pax6^+$ cell counts in (C, H) were performed. Welch's *t*-test, (A-B, D-G) N = 5. Data presented as mean ± SD. N.s., not significant; *P≤ 0.05; **P ≤ 0.01. Scale bar: Scale bar: 50µm in (A-B, D-G, F'-G'). a, anterior; Ad, anterodorsal; d, dorsal; EGL, external granular layer; Pc, preculminate; p, posterior; Pr, primary; v, ventral.

Figure 10. EdU birth dating revealed potential disruptions to tangential and radial migration of GCs in *Mllt11* cKOs. (A-N, Q-S) E18.5 medial sagittal cerebellar sections following an EdU pulse 12 hours prior to harvesting which labeled tangentially migrating and early-inwardly migrating GCs. (A) Control and (B) *Mllt11* cKO Ad lobes co-stained with DAPI. (C) β–gal staining in the RL region showed *Mllt11* locus activity in cells of the RL, EGL, and cerebellar anlage core, which overlapped where $Cux2^{CreERT2}$-mediated excision was spatially restricted, based on TdTomato fluorescence (D). (I) EdU^+ nuclei labeling revealed a larger cohort of cells populating the Ad lobe in controls versus *Mllt11* cKOs (F). (G, H) EdU in the RL region

including the inferior and posterior cardinal lobes co-stained with DAPI. (I) Control and (J) *Mllt11* cKO Ab lobes co-stained with DAPI. (K) EdU^+ nuclei in the RL and EGL of control and (L) *Mllt11* cKOs with colour-coded insets corresponding to panels below. (K') RL of controls revealed fewer EdU^+ nuclei accumulated in the RL compared to cKOs (L'). (K'') Distal EGL of controls exhibited a greater number of EdU^+ nuclei versus *Mllt11* cKOs (L''). (M) EdU^+ nuclei labeling revealed a larger cohort of cells populating the Ab lobe in controls versus *Mllt11* cKOs (N). (O) Bar graph comparison of EdU^+ nuclei in the Ab and Ad lobes of controls versus cKOs with counts normalized per 5000 μm^2 area. (Q-S) Some EdU^+ nuclei expressed the marker Pax6 which are likely inwardly migrating GCs (white arrows). (P) Line chart comparison of EdU^+ cells in bins placed in the RL (50 x 50 μm) and EGL regions (25 x 25 μm) moving distally in control versus cKO, suggested a potential tangential migratory defect. Welch's *t*-test, (A-N) N = 5. Data presented as mean ± Sd. n.s., not significant; **P ≤ 0.01; ***P ≤ 0.001. Scale bar: 50µm (A-L, M-N, Q-S), 10µm for (K'-L''). a, anterior; d, dorsal; EGL, external granular layer; p, posterior; RL, rhombic lip; v, Ventral.

Figure 11. *Mllt11* loss altered the infolding of the Purkinje plate. (A-D) Medial sagittal sections of E18.5 cerebella stained with Calbindin to label the PP beneath the EGL which formed in both controls (A, C) and *Mllt11* cKOs (B, D). (A, C) Controls exhibited a highly invaginated PP at dorsal fissures, while cKOs (B, D) were less invaginated, likely reflecting perturbed overlying fissures. (C'-D') High magnification view of the Ad lobe revealing reduced infolding of the PP in cKOs (D') compared with controls (C'). Scale: 100µm in (A-D, C'-D') a, anterior; d, dorsal; EGL, external granular layer; Mb, midbrain; p, posterior; RL, rhombic lip; v, ventral.

Figure 12. The inhibitory interneuron population was largely unaffected by *Mllt11* loss. (A-D) E18.5 Medial sagittal cerebellar sections with Pax2 staining for inhibitory INs. (A, C) Control inhibitory INs populated deeper into the developing dorsal lobes compared to *Mllt11* cKOs (B, D). (E) Schematic depicting how $Pax2^+$ cell counts were performed in each cardinal lobe (150 μm from the inner EGL surface). (F) Bar chart comparison of $Pax2^+$ cells in each identified cardinal lobe in 100 x 100 μm bins. No difference was found across cardinal lobes except in the Ad lobe which may reflect the smaller folia and accumulation of $Pax2^+$ cells in the core exhibited by cKOs. Welch's *t*-test, (A-D) N = 4. Data presented as mean ± Sd. n.s., not significant; *P ≤ 0.05. Scale: 100 μm in (A-D). a, anterior; d, dorsal; p, posterior; v, ventral.

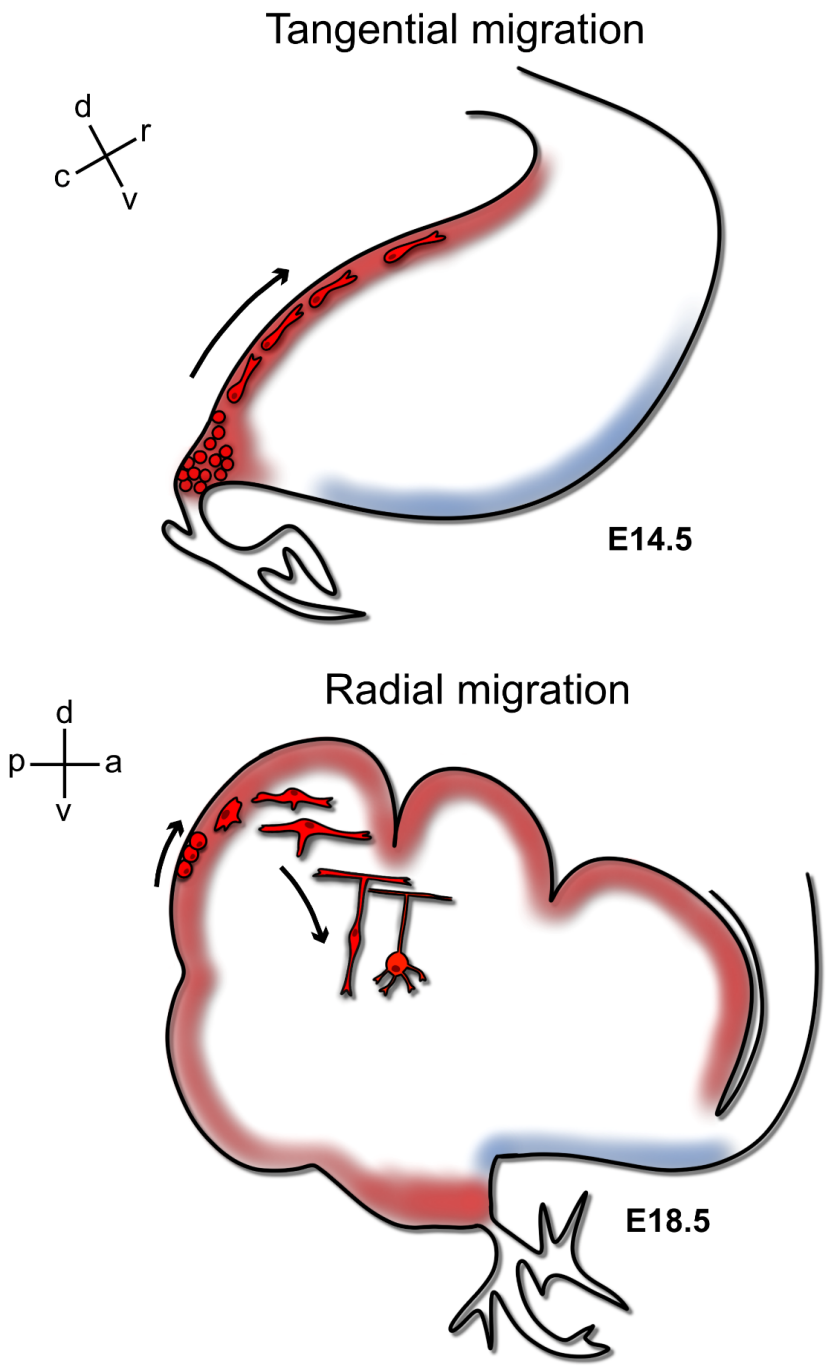
Tangential migration
d
r
c
v
E14.5
Radial migration
d
p
a
v
E18.5

Figure 1

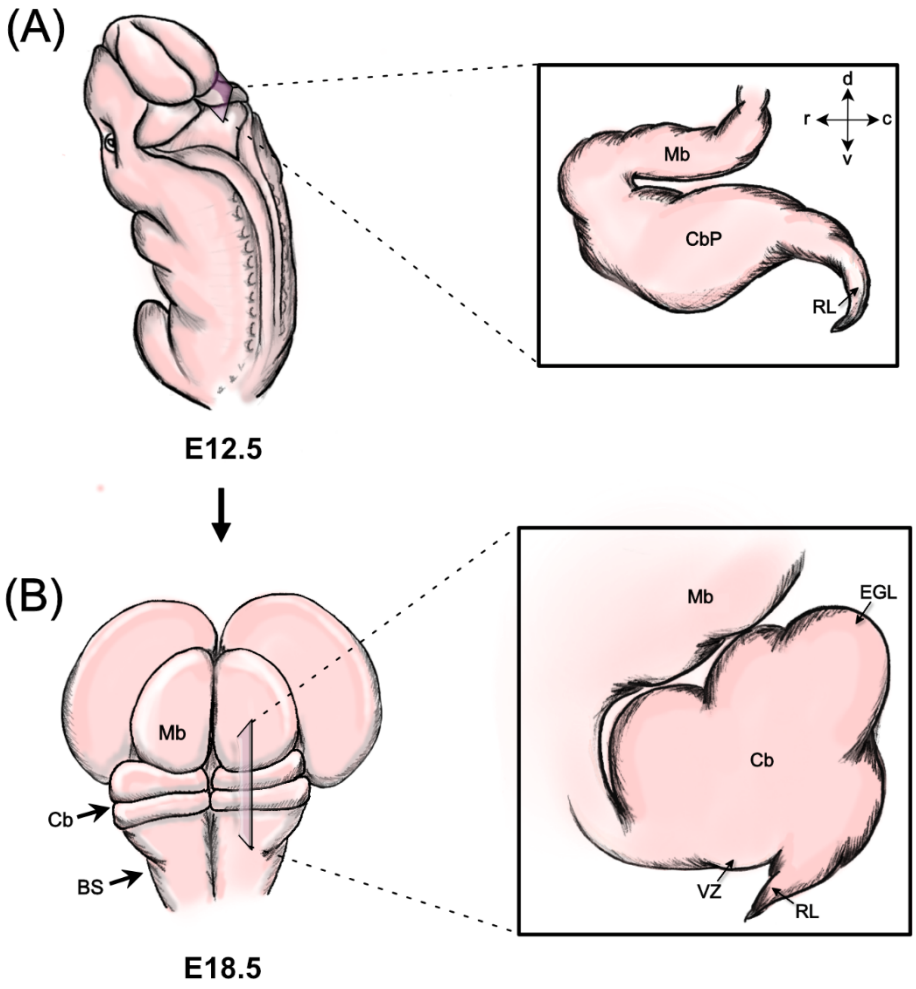

Figure 2

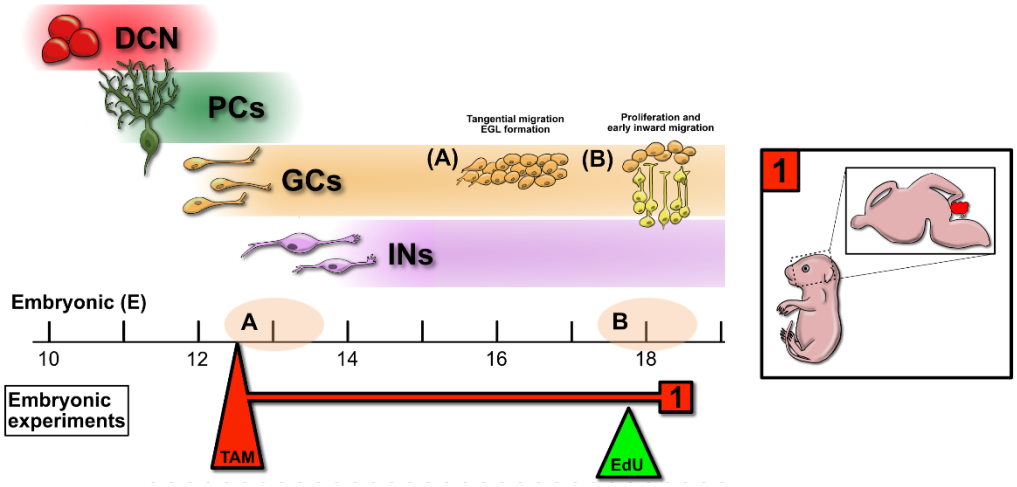
DCN
PCs
GCs
INs
Tangential migration
EGL formation
Proliferation and
early inward migration
(A)
(B)
1
Embryonic (E)
A
B
10
12
14
16
18
Embryonic
experiments
TAM
EdU
1

Figure 3

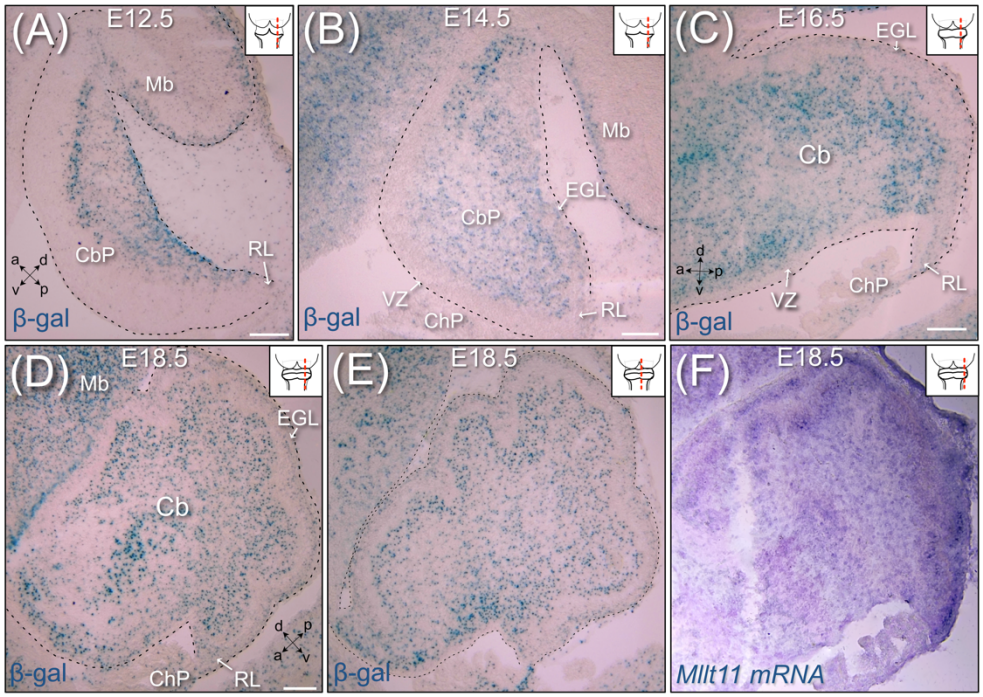
(A)
E12.5
Mb
CbP
RL
a
d
v
p
β-gal
(B)
E14.5
Mb
EGL
CbP
VZ
ChP
RL
β-gal
(C)
E16.5
EGL
Cb
d
a
p
v
VZ
ChP
RL
β-gal
(D)
E18.5
Mb
EGL
Cb
d
p
a
v
β-gal
ChP
RL
(E)
E18.5
β-gal
(F)
E18.5
Mllt11 mRNA

Figure 4

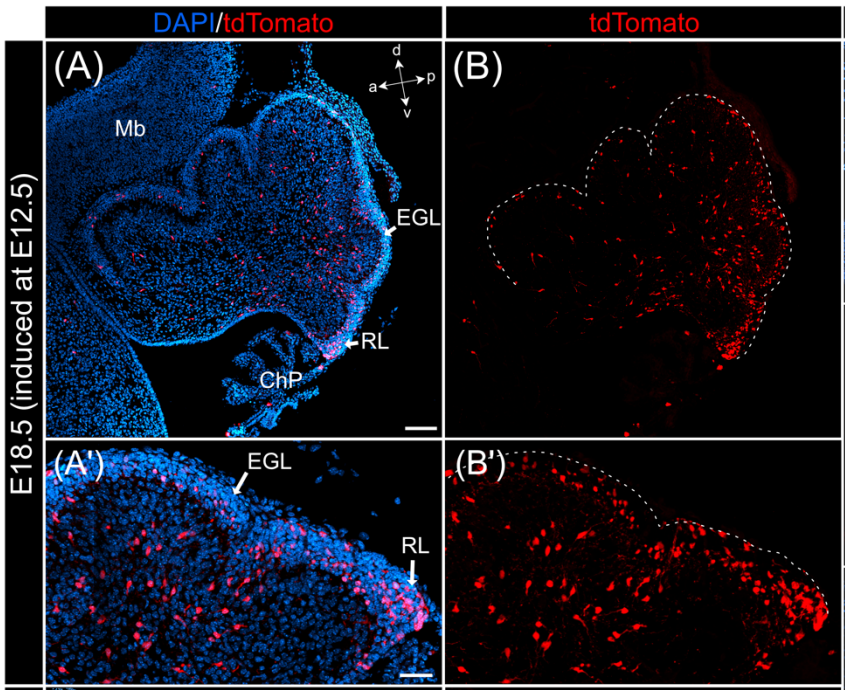
DAPI/tdTomato
tdTomato
E18.5 (induced at E12.5)
(A)
(B)
(A')
(B')
Mb
EGL
RL
ChP
d
a
p
v

Figure 5

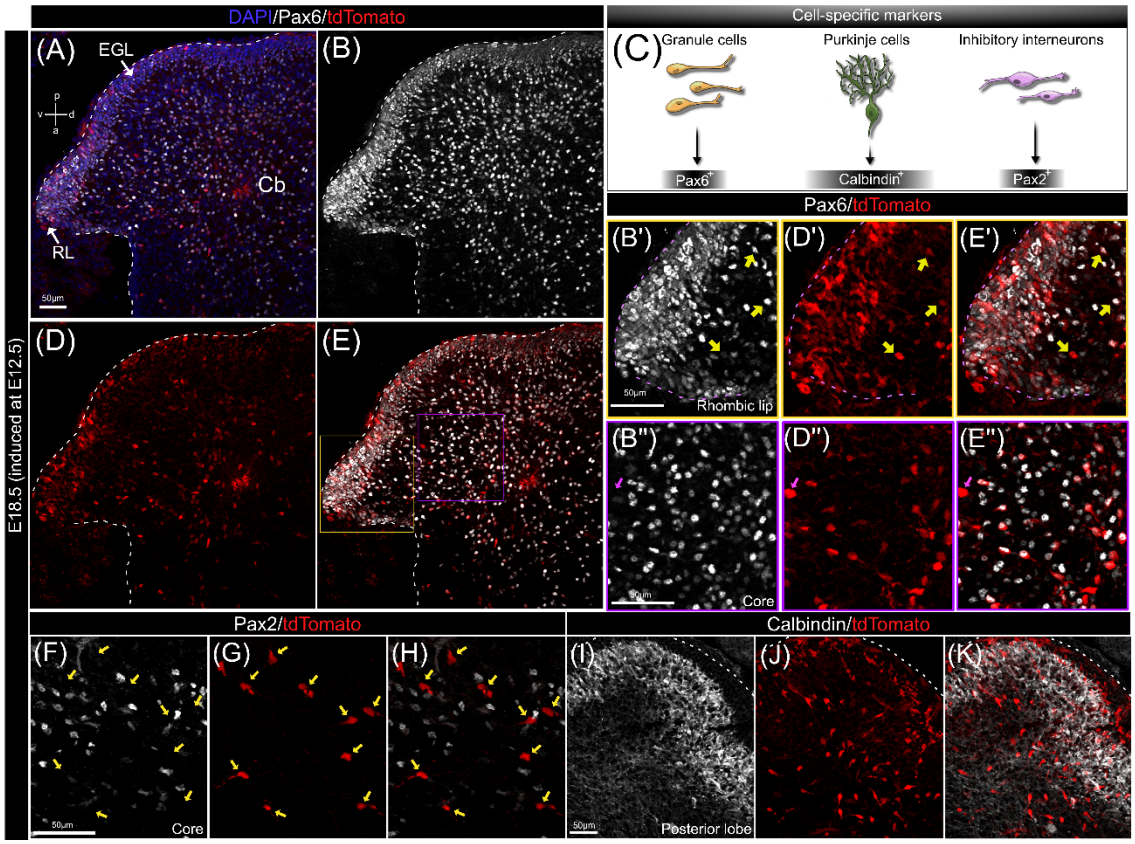
DAPI/Pax6/tdTomato
(A)
EGL
Cb
RL
50μm
(B)
(D)
(E)
E18.5 (induced at E12.5)
Cell-specific markers
(C)
Granule cells
Purkinje cells
Inhibitory interneurons
Pax6+
Calbindin+
Pax2+
Pax6/tdTomato
(B')
(D')
(E')
Rhombic lip
(B")
(D")
(E")
Core
Pax2/tdTomato
(F)
(G)
(H)
Calbindin/tdTomato
(I)
(J)
(K)
Posterior lobe

Figure 6

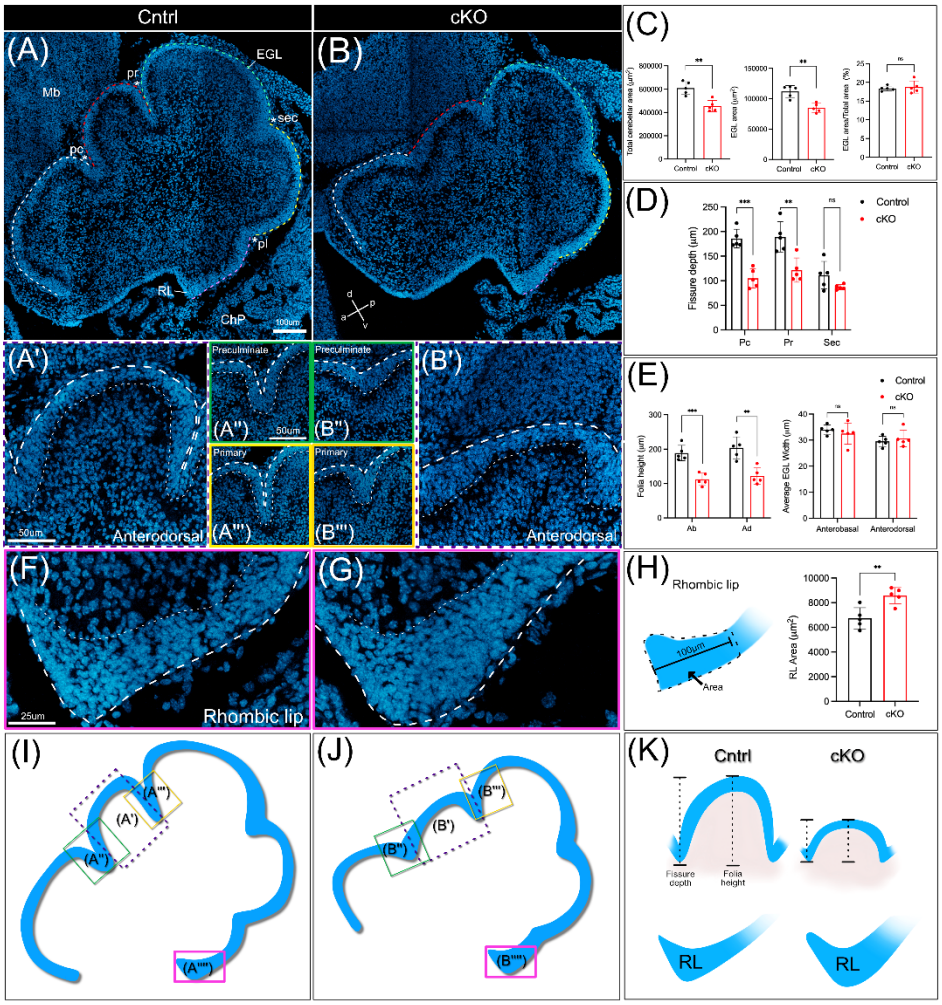
Cntrl
cKO
(A)
(B)
EGL
Mb
pr
sec
pc
pl
RL
ChP
100um
(A')
(B')
Preculminate
Primary
(A'')
(B'')
(A''')
(B''')
50um
Anterodorsal
(C)
Control
cKO
Pc
Pr
Sec
(D)
Fissure depth (μm)
(E)
Folia height (μm)
Average EGL Width (μm)
Ab
Ad
Anterobasal
Anterodorsal
(F)
(G)
25um
Rhombic lip
(H)
Rhombic lip
100um
Area
RL Area (μm²)
(I)
(J)
(A'''')
(B'''')
(K)
Cntrl
cKO
Fissure depth
Folia height
RL

Figure 7

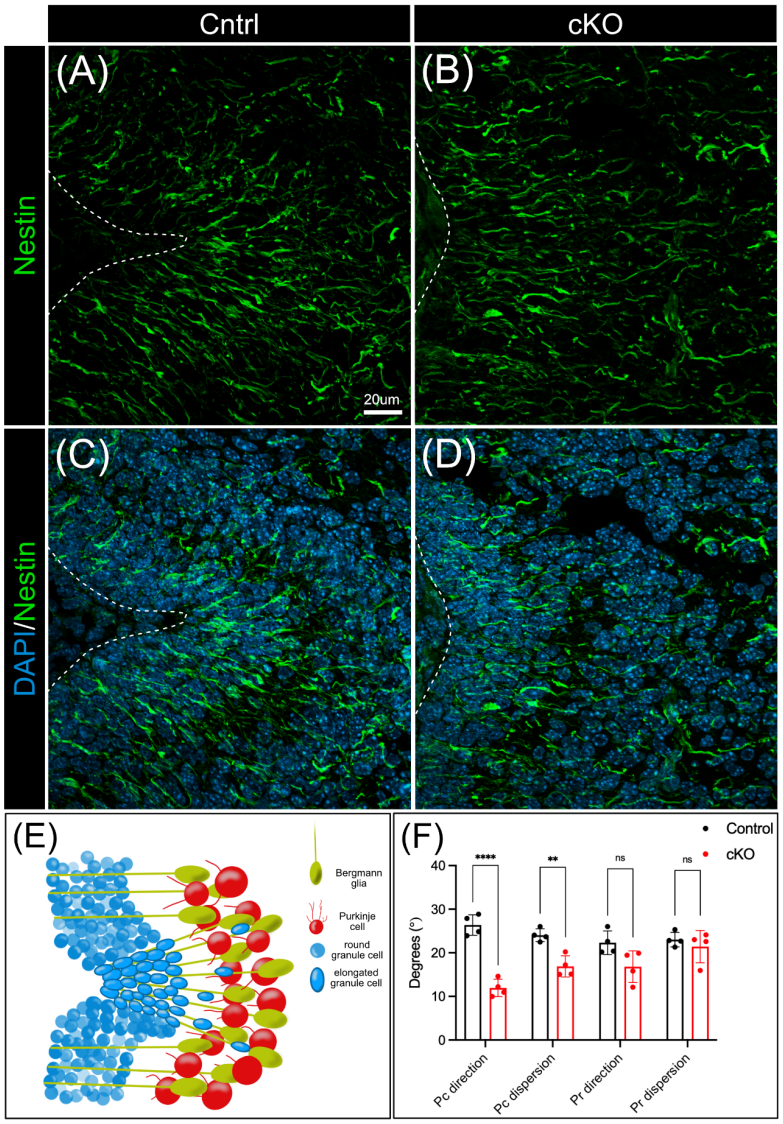
Cntrl
cKO
(A)
(B)
Nestin
20um
(C)
(D)
DAPI/Nestin
(E)
Bergmann glia
Purkinje cell
round granule cell
elongated granule cell
(F)
Control
cKO
Degrees (°)
40
30
20
10
0
****
**
ns
ns
Pc direction
Pc dispersion
Pr direction
Pr dispersion

Figure 8

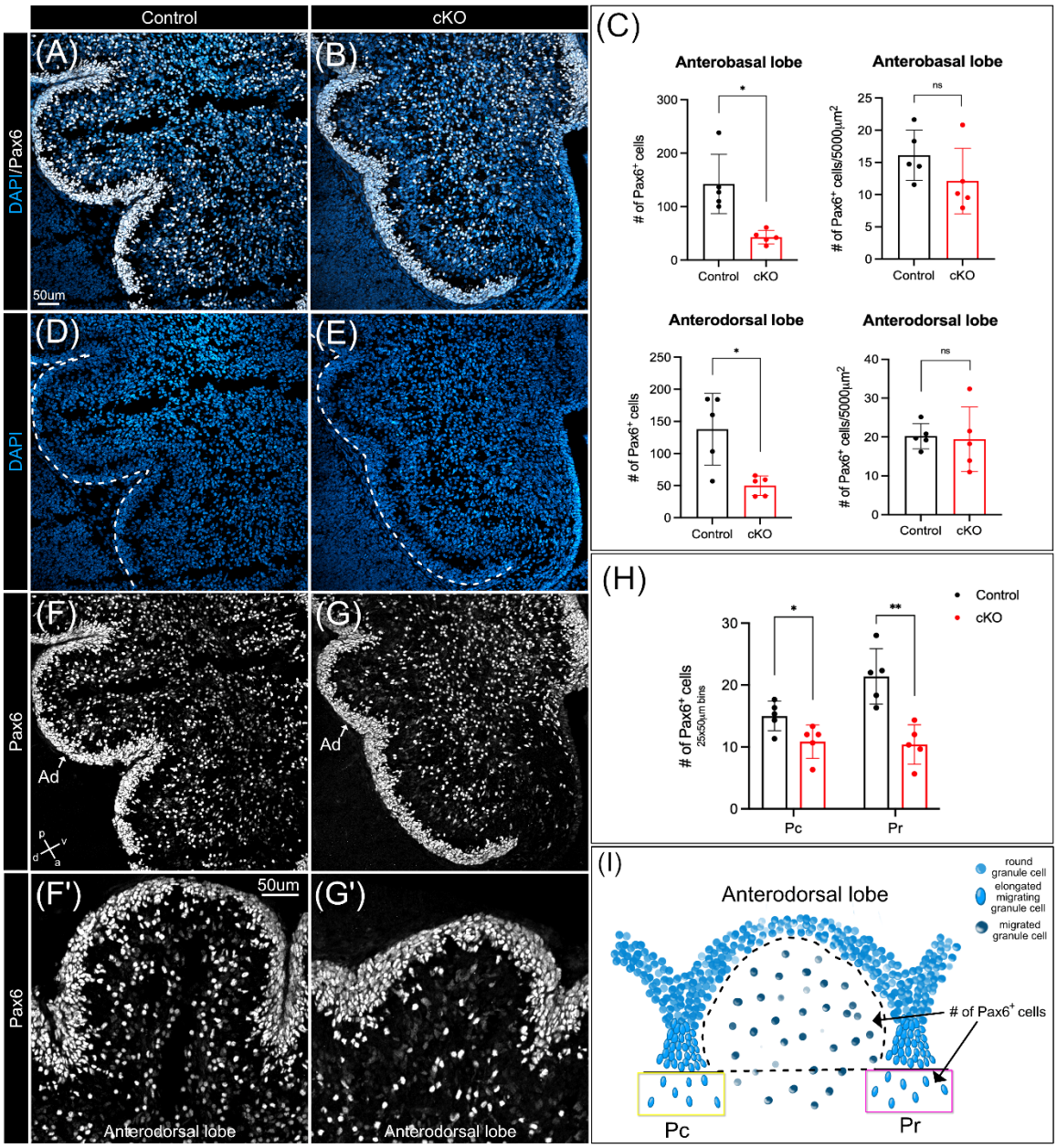
Control
cKO
(A)
(B)
DAPI/Pax6
50um
(C)
Anterobasal lobe
# of Pax6+ cells
Control
cKO
Anterobasal lobe
# of Pax6+ cells/5000μm2
ns
Anterodorsal lobe
Anterodorsal lobe
(D)
(E)
DAPI
(F)
(G)
Pax6
Ad
(H)
Control
cKO
# of Pax6+ cells
25x50μm bins
Pc
Pr
(F')
(G')
Pax6
Anterodorsal lobe
(I)
Anterodorsal lobe
round granule cell
elongated migrating granule cell
migrated granule cell
# of Pax6+ cells
Pc
Pr

Figure 9

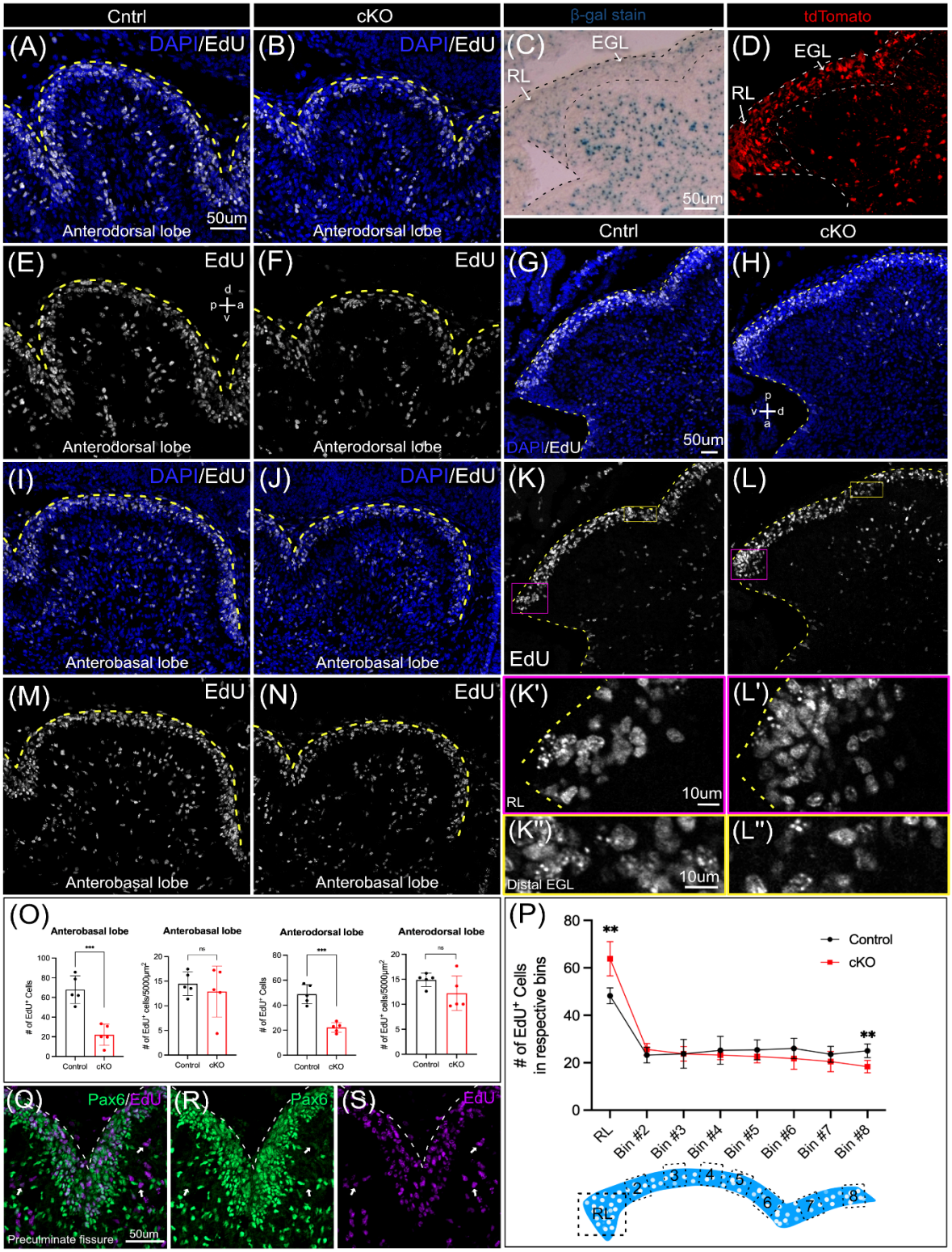
Cntrl
cKO
β-gal stain
tdTomato
(A)
DAPI/EdU
Anterodorsal lobe
50um
(B)
DAPI/EdU
Anterodorsal lobe
(C)
EGL
RL
50um
(D)
EGL
RL
(E)
EdU
Anterodorsal lobe
(F)
EdU
Anterodorsal lobe
(G)
DAPI/EdU
50um
(H)
(I)
DAPI/EdU
Anterobasal lobe
(J)
DAPI/EdU
Anterobasal lobe
(K)
EdU
(L)
(M)
EdU
Anterobasal lobe
(N)
EdU
Anterobasal lobe
(K')
RL
10um
(L')
(K'')
Distal EGL
10um
(L'')
(O)
Anterobasal lobe
Anterobasal lobe
Anterodorsal lobe
Anterodorsal lobe
# of EdU+ Cells
# of EdU+ cells/5000um2
Control
cKO
(P)
# of EdU+ Cells in respective bins
Control
cKO
RL
Bin #2
Bin #3
Bin #4
Bin #5
Bin #6
Bin #7
Bin #8
(Q)
Pax6/EdU
Precuminate fissure
50um
(R)
Pax6
(S)
EdU

Figure 10

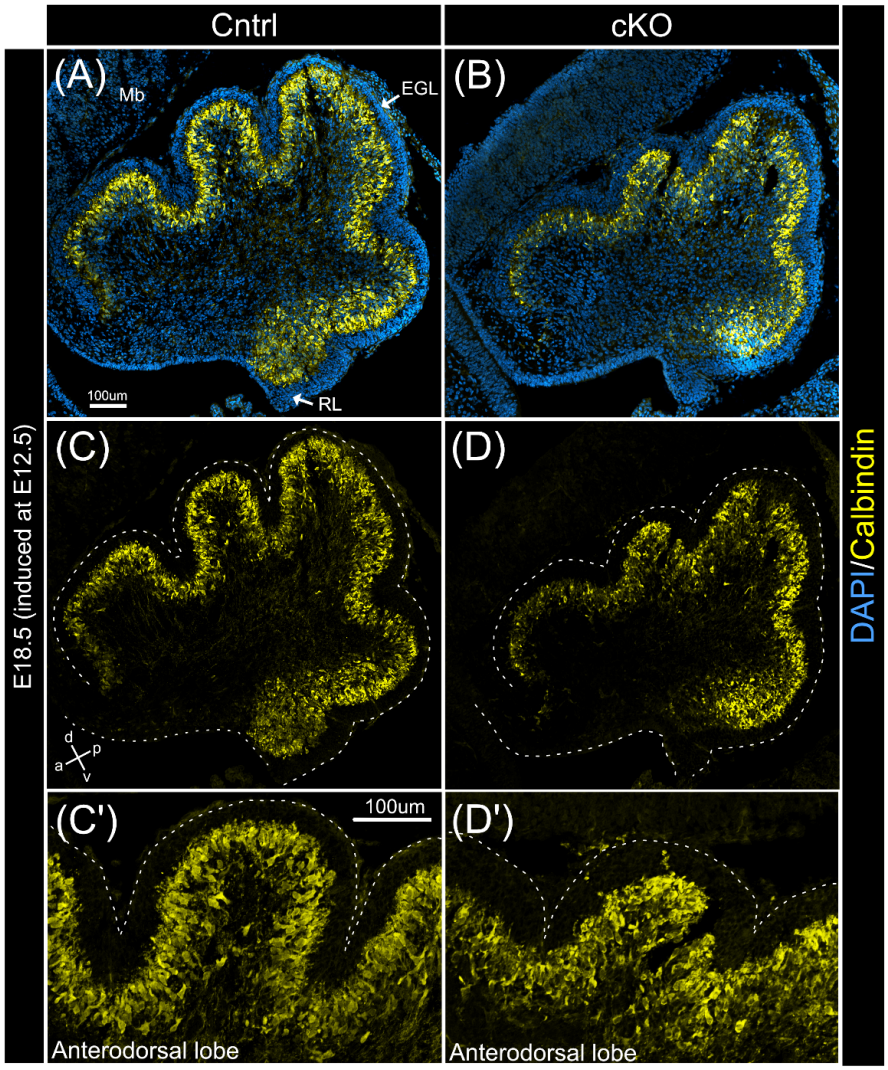
Cntrl
cKO
(A)
Mb
EGL
RL
100um
(B)
(C)
(D)
d
p
a
v
(C')
100um
(D')
Anterodorsal lobe
Anterodorsal lobe
E18.5 (induced at E12.5)
DAPI/Calbindin

Figure 11

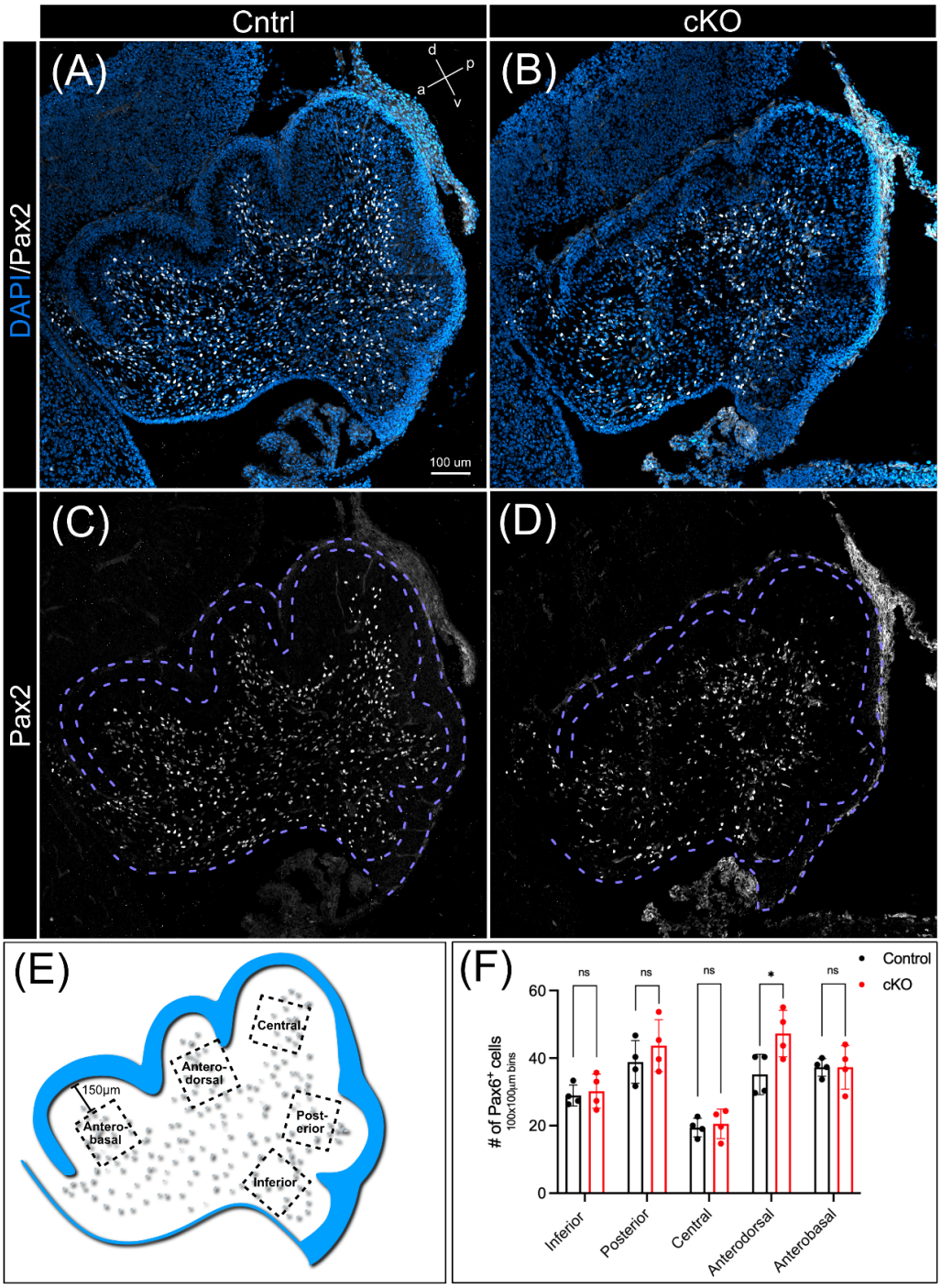
Cntrl
cKO
DAPI/Pax2
Pax2
(A)
(B)
(C)
(D)
(E)
(F)
d
p
a
v
100 um
Central
Antero-
dorsal
150µm
Antero-
basal
Post-
erior
Inferior
Control
cKO
ns
*
# of Pax6+ cells
100x100µm bins
60
40
20
0
Inferior
Posterior
Central
Anterodorsal
Anterobasal

Figure 12